Comprehensive Summaries of Uppsala Dissertations
from the Faculty of Science and Technology 651

$LiMn_2O_4$ as a Li-Ion Battery Cathode

From Bulk to Electrolyte Interface

BY

TOM ERIKSSON

ACTA UNIVERSITATIS UPSALIENSIS
UPPSALA 2001

Dissertation for the Degree of Doctor of Philosophy in Inorganic Chemistry presented at Uppsala University in 2001.

Abstract

Eriksson, T. 2001. $LiMn_2O_4$ as a Li-Ion Battery Cathode. From Bulk to Electrolyte Interface. Acta Universitatis Upsaliensis. *Comprehensive Summaries of Uppsala Dissertations from the Faculty of Science and Technology* 651. 53 pp. Uppsala. ISBN 91-554-5100-4.

$LiMn_2O_4$ is ideal as a high-capacity Li-ion battery cathode material by virtue of its low toxicity, low cost, and the high natural abundance of Mn. Surface related reactions and bulk kinetics have been the major focus of this work. The main techniques exploited have been: electrochemical cycling, X-ray diffraction, X-ray photoelectron spectroscopy, infrared spectroscopy and thermal analysis.

Interface formation between the $LiMn_2O_4$ cathode and carbonate-based electrolytes has been followed under different pre-treatment conditions. The variables have been: number of charge/discharge cycles, storage time, potential, electrolyte salt and temperature. The formation of the surface layer was found not to be governed by electrochemical cycling. The species precipitating on the surface of the cathodes at ambient temperature have been determined to comprise a mixture of organic and inorganic compounds: LiF, Li_xPF_y (or Li_xBF_y, depending on the electrolyte salt used), $Li_xPO_yF_z$ (or $Li_xBO_yF_z$) and poly(oxyethylene). Additional compounds were found at elevated temperatures: phosphorous oxides (or boron oxides) and polycarbonates. A model has been presented for the formation of these surface species at elevated temperatures.

The cathode surface structure was found to change towards a lithium-rich and Mn^{3+}-rich compound under self-discharge. The reduction of $LiMn_2O_4$, in addition to the high operating potential, induces oxidation of the electrolyte at the cathode surface.

A novel *in situ* electrochemical/structural set-up has facilitated a study of the kinetics in the $LiMn_2O_4$ electrode. The results eliminate solid-phase diffusion as the rate-limiting factor in electrochemical cycling. The electrode preparation method used results in good utilisation of the electrode, even at high discharge rates.

Keywords: cathode materials, lithium manganese oxide, interface, surface layer, electrode kinetics.

Tom Eriksson, Materials Chemistry, Ångström Laboratory, Uppsala University,
Box 538, SE-751 21 Uppsala, Sweden.

ISSN 1104-232X
ISBN 91-554-5100-4

Printed in Sweden by Eklundshofs Grafiska AB, Uppsala, 2001

Preface

This thesis comprises the present summary and the following publications, which are referred to in the summary by their Roman numerals.

I. **Surface analysis of $LiMn_2O_4$ electrodes in carbonate based electrolytes**
T. Eriksson, A.M. Andersson, A.G. Bishop, C. Gejke, T. Gustafsson, and J.O. Thomas
Accepted for publication in *J. Electrochem. Soc.*

II. **Surface structure on $LiMn_2O_4$ electrodes**
T. Eriksson, T. Gustafsson, and J.O. Thomas
Submitted to *Electrochem. Solid St. Lett.*

III. **Temperature influence on the interface chemistry of $LiMn_2O_4$ electrodes**
T. Eriksson, A.M. Andersson, C. Gejke, T. Gustafsson, and J.O. Thomas
Submitted to *Langmuir*.

IV. **Kinetic investigation of $LiMn_2O_4$ cathodes by *in situ* XRD with constant current cycling and potential steps**
T. Eriksson, A-K. Hjelm, G. Lindberg, J.O. Thomas, and T. Gustafsson
Submitted to *J. Electrochem. Soc.*

Papers of relevance to my work but not included in this thesis.

V. **Influence of carbon black and binder on Li-ion batteries**
L. Fransson, T. Eriksson, K. Edström, T. Gustafsson and J.O. Thomas
Accepted for publication in *J. Power Sources.*

VI. **A furnace for *in situ* X-ray diffraction studies of insertion processes in electrode materials at elevated temperatures**
T. Eriksson, A.M. Andersson, Ö. Bergström, K. Edström, T. Gustafsson, and J.O. Thomas
J. Appl. Cryst., in press.

VII. **An XPS study of the SEI-layer formed on an $Li_xMn_2O_4$ cathode**
T. Eriksson, T. Gustafsson, and J.O. Thomas
in *Lithium Batteries*, S. Surampudi and R. Marsh, Eds., PV 98-16, The Electrochemical Society Proceedings Series, Pennington, NJ, 1998, p. 315

VIII. **Measurement of electrochemical stability of gel electrolytes for lithium batteries**
P. Georén, T. Eriksson, L. Fransson, P. Gavelin, K. Edström, T. Gustafsson, P. Jannasch, and G. Lindberg
In manuscript.

My contribution to the papers in this thesis

Paper I: Planning of all experiments; all electrochemical measurements; XPS measurements with A.M. Andersson; SEM measurements; evaluation of data (IR together with C. Gejke) except Raman measurements; writing the manuscript excluding the Raman part.

Paper II: Planning of all experiments; all electrochemical measurements; XPS measurements with A.M. Andersson; SEM, XRD and DSC measurements; evaluation of all data (IR with C. Gejke); writing the manuscript.

Paper III: All the planning, measurements, evaluation and writing.

Paper IV: Planning and performing of all experiments in collaboration with A-K. Hjelm; XRD data evaluation; electrochemical evaluation (excluding transient simulations) and writing the manuscript together with A-K. Hjelm.

CONTENTS

1. THE SCOPE OF THE THESIS

"…its five year mission: to explore strange new worlds, to seek out new life, and new civilizations, to boldly go where no man has gone before."

- Captain Kirk

Capacity losses in electrochemical systems may originate in several mechanisms. It is important to understand these mechanisms in order to eliminate them and thus improve capacity retention. One of the possible trouble-spots is the interface between electrode and electrolyte. This is an area where fundamental knowledge is lacking as stated by P.G. Bruce: "All electrochemical devices rely on the performance of the interfaces between electrolytes and electrodes, at least as much as on the performance of the bulk phases. As a result interfacial studies are growing rapidly in importance. This has only served to emphasise how little is presently understood concerning the fundamental processes at such interfaces." [1]

There has been much research on the reduction of electrolyte, and the formation of a solid electrolyte interface (SEI) on the negative electrode in the Li-ion battery. [2] However, on the positive-electrode side, there is a corresponding oxidation of the electrolyte and this has been neglected, although the phenomenon is well known. [3,4] This was pointed out in the review article by Arora *et al.*: "Considering the large number of studies on solvent reduction in lithium batteries, and the relative importance of solvent oxidation to cell performance and safety, the lack of fundamental knowledge in this area is surprising." [5]

At slightly elevated temperatures, the interface reactions between electrolyte and the active cathode material becomes a true problem, with increasing cell-impedance, capacity losses and lowered rate capability as a consequence. In the long run, it presents a security hazard for the battery, where secondary reactions may lead to thermal runaway with detrimental effects on both battery and the potential user. This present work tries to shed some light on the reactions and products formed on the composite cathode electrode surface, as well as investigating the kinetic limitations of this electrode.

Questions asked:

- Is a surface film produced on the cathode by processes connected with cell-cycling in a Li-ion cell, equivalent to the graphite anode case?
- What species are formed at the $LiMn_2O_4$/electrolyte interface?
- How does temperature influence the interface chemistry of a $LiMn_2O_4$ cathode?
- In what way does the active cathode material contribute to the interface reactions?
- What is the rate-limiting step in the lithium removal/insertion in $LiMn_2O_4$?

Answers to these questions were sought through the use of analytical methods: X-ray photoelectron spectroscopy (XPS), X-ray diffraction (XRD), infrared spectroscopy (IR), scanning electron microscopy (SEM) and differential scanning calorimetry (DSC), together with electrochemical methods: chronoamperometry (potentiostatic measurement) and chronopotentiometry (galvanostatic measurement).

2. INTRODUCTION

"Powerhouse of energy, whipping up a fury, dominating flurry, we create the Battery"

-Metallica

2.1 Elementary battery concepts

A battery is a device that converts chemical energy into electrical energy by means of an electrochemical reduction-oxidation (redox) reaction.

With the ever-increasing market for portable electronic devices, e.g. cell-phones, laptop computers, there is also an increased need for improved energy sources. Most of the electronic products today use "state-of-the-art" batteries, and yet the performance of these leaves much to be desired. Another aspect is the environmental threat posed by the heavy metals used in many of today's battery concepts. As society is becoming more aware of these problems, the desire for environmentally friendly battery components is growing.

The historical battery development has gone from copper/zinc (Volta, 1800), lead-acid (Planté, 1859) and zinc/manganese-oxide (Leclanché, 1866) over zinc-air (1878), Ni-Cd (Jungner, 1899), sodium-sulphur (Yao & Kummer, 1966) and Li primary cells (1960's) to the present technology of Ni-MH (early 1980's) and Li-ion secondary cells (early 1990's). [6]

There are two types of batteries: primary and secondary. In primary batteries, the electrode reactions are not reversible and the cells are therefore not rechargeable, *i.e.* after one discharge, they are discarded. In secondary batteries, the electrode reactions are reversible and the cells are rechargeable.

A battery comprises three main components: cathode, electrolyte and anode. The cathode is characterised as the electrode where a reduction-reaction occurs (*i.e.* electrons are accepted from an outer circuit), while an oxidation-reaction occurs at the anode (*i.e.* electrons are donated to an outer circuit). The electrolyte is an electronic insulator, but a good ionic conductor; its main function is to provide a transport-medium for ions to travel from one electrode to the other. It must also prevent short-circuiting by acting as a physical barrier between the electrodes, either alone in the case of a polymer or in the matrix it impregnates (the separator) if a liquid. The voltage and capacity of a cell are functions of the electrode materials used.

Example of typical electrode reactions, exemplified by the lead-acid battery:

Anode	$Pb + H_2SO_4 \rightarrow PbSO_4 + 2H^+ + 2e^-$
Cathode	$PbO_2 + H_2SO_4 + 2H^+ + 2e^- \rightarrow PbSO_4 + 2H_2O$
Total cell reaction	$Pb + PbO_2 + 2H_2SO_4 \rightarrow 2PbSO_4 + 2H_2O$

Definition of terms used:
Capacity (C or Ah): Total amount of charge involved in the electrochemical reaction
Specific capacity (Ah/kg): Capacity per mass unit
Volumetric capacity (Ah/l): Capacity per volume unit
Energy (J or Wh): Amount of electrical work done = U x I x t
Specific energy (Wh/kg): Energy per mass unit
Energy density (Wh/l): Energy per volume unit
Power (W): Rate at which the energy is available = U x I
Charge or discharge rate (C/h): h is the number of hours needed for completing of one charge or discharge

Consider the total cell-reaction: $Li_xMn_2O_4 + Li_yC_6 \leftrightarrow Li_{x+\delta}Mn_2O_4 + Li_{y-\delta}C_6$

The thermodynamic quantity describing the change in energy as a function of changes in Li concentration in the host matrix is the chemical potential (μ), defined as

$$\mu = \frac{\partial G}{\partial x} \tag{1}$$

where G is the Gibbs free energy and x is the number of inserted Li atoms. The change in free energy can also be expressed as:

$$\Delta G = -nFE = -\delta FE \tag{2}$$

where n is the number of electrons in both electrode-reactions (δ in the cell-reaction above), F is Faraday's constant, and E is the potential difference between the electrodes. By combining (1) and (2), we get the relation between electrical and chemical energy in the system:

$$-\delta FE = \mu_c - \mu_a \tag{3}$$

where μ_c and μ_a are the chemical potentials of the lithium ions in the cathode and anode, respectively.

2.2 The Li-ion battery

The most advanced batteries on the market today are the Li-ion and Li-ion-polymer batteries. [7,8] Although the history of batteries spans more than 200 years, there have been long periods of inactivity between the revolutionary advances. A lot of academic and commercial effort has been expended, for example, in trying to incorporate a manganese-oxide electrode, used already in the early Leclanché battery, into the modern technology of secondary lithium-batteries. It may seem like a straightforward task but, as will be seen later, secondary processes occurring in the cell during reversible cycling complicates the situation.

One of the last century's most revolutionary battery-related discoveries was the interaction between alkali-metal-salts and polar polymers. [9] These compounds exhibit significant ionic conductivity and prompted Armand *et al.* to make a more detailed electrical characterisation, [10,11] which led to the idea of the all-solid-state lithium-polymer battery concept. Originally, Li-metal was used as anode in the secondary Li-batteries, and an inorganic intercalation or insertion compound as cathode. The first secondary Li/insertion-compound system was the Li/TiS_2 system, [12] announced to be commercialized by Exxon in the mid 1970's.

There are advantages with using metallic Li as anode in the battery: the redox potential becomes very low and the equivalent weight is also low. There are problems, however, associated with the use of metallic Li: *e.g.* corrosion of Li by reaction with electrolyte, safety aspects where dendrite formation can cause short-circuiting of the cell with a following thermal runaway and possible explosion. The concept of Li ion transfer cells was proposed to solve these problems. [13] Nowadays, these are usually referred to as Li-ion cells. [14] In these cells, an insertion electrode, usually carbon-based, [15] replaces the Li metal anode. In this way, the active lithium is always present as an ion rather than as a metal. Metallic lithium is highly reactive with oxygen, nitrogen and moisture, making it a difficult material to handle; glove-boxes or dry-rooms become a necessity in production.

Battery production can be simplified by using insertion electrodes as both anode and cathode, since the battery components can be produced in ambient atmosphere and then swelled with electrolyte in a controlled atmosphere. [16] Electrode materials other than insertion compounds have also showed promising properties, *e.g.* polymeric cathodes [17] and nano-particle anodes. [18]

To make a complete Li-ion cell, one of the electrodes will have to contain Li-ions, which are then shuttled reversibly between the electrodes during charge/discharge. A variety of electrodes have been tested over the years [19-21] but, for commercial purposes, the $LiCoO_2$ electrode or variations thereof has been the most exploited.

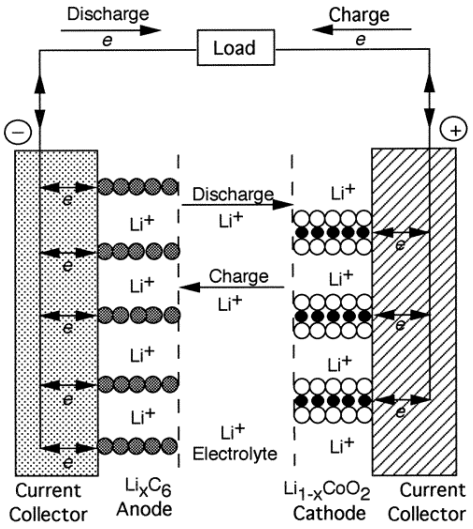

Figure 2.1 The discharge process in a rechargeable Li-ion battery. [22]

A big problem with the Li-ion concept is that any Li consumed by secondary reactions cannot be retrieved, and the specific capacity is totally dependent on the amount of Li available for the reversible redox process in the cell. Some of the processes known to lead to capacity loss in Li-ion cells are: Li deposition (in cell over-charge), electrolyte decomposition, active material dissolution, phase changes in the insertion electrode materials, and passive film formation on the electrode and current collector surfaces.

The distinguishing features of today's commercial Li-ion batteries are: [23]

- High operating voltage: a single cell has an average operating potential of approx. 3.6 V, three times the operating voltage of both Ni-Cd and Ni-MH batteries and about twice that of sealed Pb-acid batteries.
- Compact, lightweight, and high energy density: the energy density is about 1.5 times and specific energy is about twice that of high-capacity Ni-Cd batteries.
- Fast charging potential; batteries can be charged to about 80-90% of full capacity in one hour.
- High discharge rate: up to 3C are attainable.
- Wide range of operating temperature: from –20 to +60°C.
- Superior cycle life: service life of a battery exceeds 500 cycles.
- Excellent safety: United States Department of Transportation, Dangerous Materials Division has declared Li-ion batteries exempt from dangerous materials regulations.
- Low self-discharge: only 8-12% per month.
- Long shelf-life: no reconditioning required up to approximately 5 years (Ni-Cd: 3 months; Ni-MH: 1 month).
- No memory-effect: can be recharged at any time.
- Non-polluting: does not use toxic heavy metals such as Pb, Cd or Hg.

2.3 Insertion electrodes

An insertion compound is a solid host network incorporating guest ions. It has two specific properties which makes it different from a normal solid structure: the guest ions are mobile between sites in the host network, and the guest-ions can be removed from or added to the host network, thus varying the guest-ion concentration. An insertion compound is an ionic and electronic conductor, and the uptake or release of electrons compensates for a change in guest-ion concentration. In Li-ion batteries, Li^+ is the guest ion and the host network comprises transition-metal-oxides (TMO's), other transition-metal-chalcogenides (sulphides, selenides, or tellurides) or transition-metal salts with oxoanions (*e.g.* phosphate, sulphate or arsenate).

For transition-metal oxides and other chalcogenides, positive guests (like Li^+) occupy sites surrounded by negative oxygen or chalcogen ions. The guest ions strive to stay as far away as possible from the positive transition-metal ions. The sites available to the Li-ion are determined by the host structure. The first experimental investigation of a lithium insertion compound was on the Li_xTiS_2 structure. [12] It has later been established that TMO's are more attractive candidates for insertion electrodes. [24] This is mainly due to their higher potential *vs.* Li/Li^+ – giving a high specific energy – and their excellent reversibility.

The term "intercalation" is sometimes used in the literature; it implies a special case where "insertion" occurs into a layered host matrix, which retains its structural integrity during the intercalation process. This is the case, for example, for graphite, $LiCoO_2$ and $LiNiO_2$.

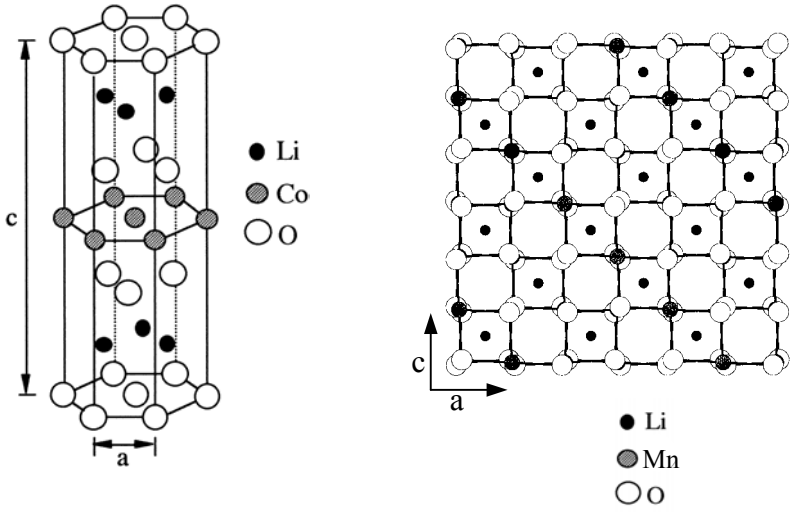

Figure 2.2 A. Two-dimensional layered host with α-$NaFeO_2$ -type structure. B. Three-dimensional framework host with cubic spinel $MgAl_2O_4$ -type structure.

The simplest and most studied insertion-compound structures contain close-packed arrays of oxygen with the transition-metal (*M*) atoms occupying half of the octahedral sites. These compounds are either layered ($LiMO_2$) (Fig. 2.2 A) or framework (LiM_2O_4) type (Fig. 2.2 B).

The theoretical capacity of a material can easily be calculated from Faraday's 1st law of electrochemistry, which states that 1 gram equivalent weight of a material will deliver 96487 coulombs (or 26.8 Ah). This can be very useful when considering the synthesis of new materials. It can readily be assessed whether the material can compete with existing electrode materials in terms of specific capacity. For $LiMn_2O_4$ the equivalent weight (M) is 180.8 g/mol, giving a theoretical capacity of: 26.8/180.8 = 148 mAh/g. In the same way, the theoretical capacity of $Li_2Mn_2O_4$ can be determined to 285 mAh/g, if the whole charge/discharge range is exploited.

The ideal properties for an insertion electrode in a Li-ion cell are: [25,26]

- Large ΔG for the total cell reaction to provide a high cell voltage (see Eq. 2 below).
- Limited change in ΔG over the useful range of inserted Li-ions to ensure a stable operating voltage.
- Minimal changes in the host network to ensure good reversibility.
- Light host structure that is able to accommodate a significant amount of Li to provide a high capacity.
- Good electronic and ionic conductivity to provide high rate capability.
- Chemically and structurally stable over the whole voltage range and insoluble in the electrolyte.
- Inexpensive and non-toxic.
- Low oxidation potential for a fully charged positive electrode (high voltage *vs.* Li/Li^+); high oxidation potential for a fully charged negative electrode.

3. INTERFACE CHEMISTRY IN Li-ION BATTERIES

"Imagination is more important than knowledge."

- Albert Einstein

3.1 The anode SEI layer

As stated in Chapter 1, the spontaneous formation of a protective SEI layer on metallic Li was discovered by Peled in 1979. [2] Since then, a vast number of papers have been published on the non-aqueous electrochemistry of Li and graphite. [27] The electrochemical reduction reactions on graphite surfaces are similar to those on metallic Li, since the potential difference between fully intercalated graphite (LiC_6) and Li is very small. Li-C intercalation compounds are thermodynamically unstable in all known electrolytes. They are kinetically protected by the SEI films formed on exposure to the electrolyte, or during the first reduction (Li intercalation) reaction.

It is of outmost importance to produce a surface layer that is dense enough to prevent solvents from penetrating to the active electrode surface and, in this way, prevent further electrolyte reduction and ultimately electrolyte depletion in the forthcoming cycles. The reduction reactions must also be minimized to reduce gas evolution in the cell; gas formed from the reduction of electrolyte increases the internal pressure in the cell. This is hazardous in a functioning battery in a sensitive environment, *e.g.* in a working cell-phone. A problem with the formation of a protective SEI film is that it consumes Li irreversibly, with consequent loss of specific capacity in the cell. It would therefore be desirable to form the protective film prior to assembling the cell.

A thin inorganic layer covering the entire electrode provides a highly passivating film, while the impedance remains low and Li ions are still able to penetrate. [27] This is the ideal situation for an SEI layer; it is desirable to obtain a layer of *e.g.* Li_2CO_3 and LiOH closest to the electrode surface (Fig. 3.1). [28]

The thickness of the anode SEI layer has been a popular topic of debate. Anything from a few nanometers [29,30] to a few hundred nanometers [31] has been suggested. Both figures are probably correct, with the stable salts closest to the active electrode surface in the lower thickness regime, followed by a much thicker outer organic layer.

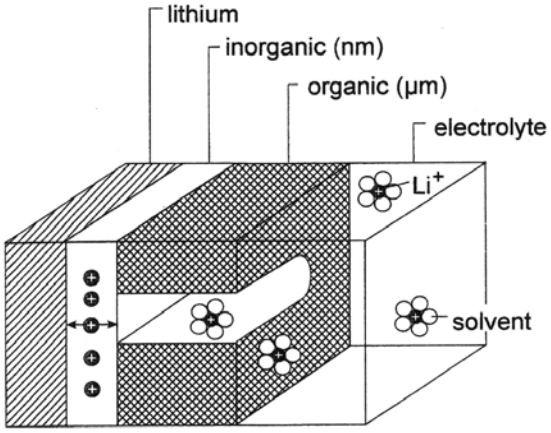

Figure 3.1 Schematic illustration of the SEI formed on Li and graphite during the first reduction reaction. [20]

3.2 Solvents and salts

There is a huge variety of solvents and salts used as liquid electrolytes, or as components in gel-type electrolytes, *e.g.* alkyl carbonates: propylene carbonate (PC), ethylene carbonate (EC)/dimethylene carbonate (DMC); esters: γ-butyrolactone (γ-BL), methylacetate (MA); ethers: 1,2-dimethoxyethane (DME), and tetrahydrofuran (THF). PC is liquid at room-temperature and exhibits good ionic conductivity and is comparatively cheap. It co-intercalates with the Li-ions in graphite, however, and cannot be used in Li-ion cells unless the graphite-surface is modified, or one uses additives in the electrolyte. This is also the problem with many other solvents, like γ-BL, DMC and THF. The esters have been investigated by Aurbach *et al.*, and were found to be too reactive towards Li, and their reaction products are of relatively low passivation. [32] Ethers are more readily oxidized on the cathode side since their α-hydrogens are highly susceptible to oxidation whereas carbonates, for example, are relatively inert to this reaction. [33]

It has been shown that the mixture EC/DMC has very good conductive properties and, most importantly, produces the best protective surface film on graphite electrodes, thus minimizing the solvent co-intercalation. [34,35] This is due to the products formed from EC, which decompose to a Li-alkyl-carbonate, $(CH_2OCO_2Li)_2$, during reduction. [34,35] $(CH_2OCO_2Li)_2$ can be formed from EC either by disporportionation of the anion radical (formed by a single electron transfer to EC), or by a two-electron transfer which form CO_3^{2-} which further attacks nucleophilically another EC molecule (Scheme 3.1). [36] EC is a solid at room-temperature and melts at 36.2°C; it is therefore necessary to have a co-solvent in the electrolyte to reduce its viscosity sufficiently for practical use. DMC, ethylene methylene carbonate (EMC) and diethylene carbonate (DEC) are common co-

solvents for EC. It has been shown that DMC is a better co-solvent for EC than, for example, DEC as regards the formation of a protective SEI film. [37]

The choice of electrolyte salt is also important. The most commonly used salts are: $LiPF_6$, $LiBF_4$, $LiAsF_6$, $LiClO_4$, $LiCF_3SO_3$ (Li-triflate) and $LiN(CF_3SO_2)_2$ (commonly known as LiTFSI). These all have different advantages and disadvantages. $LiClO_4$ is highly explosive as a precipitate in contact with organic material, and $LiAsF_6$ is very toxic. Both can therefore be ruled out for commercial applications. LiTFSI performs well, but corrodes the Al cathode current-collector with a pit-corrosion potential of 3.55 V *vs.* Li/Li^+. [38] $LiPF_6$ and $LiBF_4$ result in more acidic electrolytes due to their sensitivity to moisture, especially $LiPF_6$ (Scheme 3.2). This may affect the cathode (see later). $LiBF_4$ has a lower onset temperature for the SEI breakdown on the graphite anode, making it less suitable at the anode. A common undesirable by-product of using the inorganic fluorinated salts is LiF (Scheme 3.2), which increases the cell-impedance. The conclusion must be that $LiBF_4$ is the best salt at the cathode, while $LiPF_6$ performs best at the anode. The choice of optimal electrolyte salt will therefore be a compromise.

a) $2\ CH_2OCO_2CH_2 \xrightarrow{2Li^+,2e^-} (CH_2OCO_2Li)_2\downarrow + CH_2{=}CH_2\uparrow$

b) $2\ CH_2OCO_2CH_2 \xrightarrow{2Li^+,2e^-} LiOCO_2(CH_2)_4OCO_2Li$

c) $CH_2OCO_2CH_2 \xrightarrow{2Li^+,2e^-} Li_2CO_3\downarrow + CH_2{=}CH_2\uparrow$

d) $CH_2OCO_2CH_2 + Li_2O \xrightarrow{?} LiOCH_2CH_2OCO_2Li$

e) $2n\ (CH_2OCO_2CH_2) \longrightarrow -[(CH_2CH_2O)_x\text{-}/\text{-}(CH_2CH_2OCO_2)_y]_n- + nx\ CO_2$

f) $n\ CH_2{=}CH_2\downarrow \longrightarrow (CH_2CH_2)_n\downarrow$

g) $CH_3OCO_2CH_3 \xrightarrow{Li^+,e^-} CH_3OCO_2Li\downarrow + CH_3^{\bullet}$

h) $2\ ROCO_2Li + H_2O \longrightarrow Li_2CO_3 + 2\ ROH + CO_2$

i) $R^{\bullet} + Li^{\circ} \longrightarrow R - Li$

Scheme 3.1 Possible reactions involving alkyl-carbonates. [35,39,40]

a) $PF_6^- + 3Li^+ + 2e^- \longrightarrow 3\ LiF\downarrow + PF_3$

b) $LiPF_6 \longleftrightarrow LiF + PF_5$

c) $PF_5 + H_2O \longrightarrow POF_3 + 2HF$

d) $PF_5 + 2xLi^+ + 2xe^- \longrightarrow Li_xPF_{5-x}\downarrow + xLiF\downarrow$

e) $POF_3 + 2xLi^+ + 2xe^- \longrightarrow Li_xPOF_{3-x}\downarrow + xLIF\downarrow$

f) $BF_4^- \xrightarrow{Li^+,e^-} LiF\downarrow, Li_xBF_y\downarrow$ (in general)

Scheme 3.2 Possible reactions involving $LiPF_6$ and $LiBF_4$ reduction or decomposition. [35]

3.3 The cathode surface layer

In this thesis work we focus on the widely used carbonate-based EC/DMC electrolyte solvents. This is because PC cannot yet be used commercially. The oxidation of PC at electrode surfaces has been studied earlier [41,42] whereas, to the best of our knowledge, the oxidation of EC and DMC had never been studied prior to 1998. [43]

Aurbach *et al.* have studied the oxidation of EC/DMC and various salts at $LiNiO_2$ and $LiMn_2O_4$ composite electrodes by means of IR spectroscopy and XPS. [43,44] They find the presence of a native Li_2CO_3 film. After cycling, they find $ROCO_2Li$ species and possible polycarbonates. They report that the surface chemistry is developed during cycling and not during storage. As discussed in **Paper I** the surface film formation may be different, depending on whether a native film is present on the surface of the active cathode particles.

Du Pasquier *et al.* have studied the storage performance of $Li_{1.05}Mn_{1.95}O_4$ electrodes. [45] They performed IR spectroscopy on powder stored in EC/DMC and various salts at 100°C and found the presence of an organic surface film, possibly of a polymeric nature. Matsuo *et al.* looked at $LiMn_2O_4$ electrodes in EC/DMC $LiPF_6$ at elevated temperatures. [46] They used spin-coated thin-films, however, and the results are somewhat different from commercially used composite electrodes, *e.g.* partial dissolution and pit-corrosion after one day at 60°C. Nevertheless, the results are interesting, and their Raman measurements suggest polynuclear carbonyl complexes. An excess of electrolyte has been used in both these studies. The amount of electrolyte is crucial to the dissolution of Mn from $LiMn_2O_4$ (described in Ch. 4.3). The conditions of this present study have been designed to resemble as closely as possible those of a functioning battery.

4. PROPERTIES OF THE $LiMn_2O_4$ SYSTEM

"During the antiquity the names *magnesia* or *magnes* was given to some different minerals, *e.g.* MnO_2. The mineral was used as a decolourising agent for glass, which was the probable cause for that its name, in connection with the Greek verb μανγανιζειν = purify, later sometimes translated to *manganes*."

- Gunnar Hägg [47] (free translation from Swedish)

4.1 Structures

A part of the Li-Mn-O phase-diagram is described in Fig. 4.1. It is seen to involve a multitude of structures and tie-lines; this is related to the nature of Mn, which can have oxidation states II-VII. The most important oxidation states are II, IV and VII, with II the most stable. For Mn compounds with oxidation states II-IV octahedral coordination are the most common. [47] From a battery viewpoint, the spinel structures of interest in the Li-Mn-O phase-diagram are located within the triangle of the MnO_2–$LiMn_2O_4$–$Li_4Mn_5O_{12}$ tie-lines.

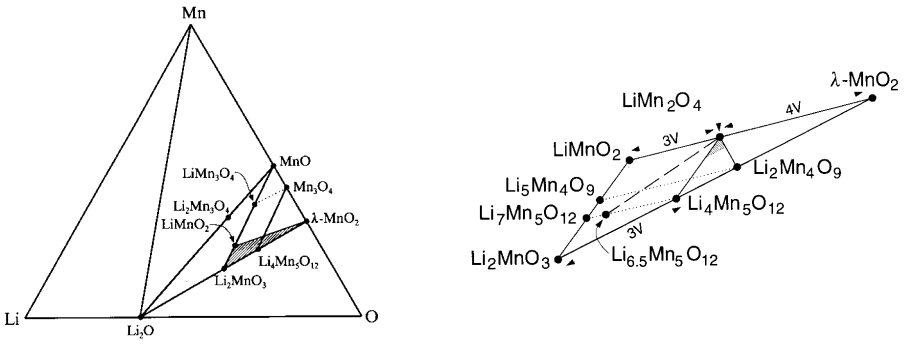

Figure 4.1 A. The Li–Mn–O phase diagram. B. A close-up of the Li_2MnO_3 – $LiMnO_2$ – λ-MnO_2 part of the Li-Mn-O phase diagram. [48]

The phases of interest in this thesis, and which can be found in electrodes after prolonged cycling or storage, elevated temperature treatments or fast charge/discharge, are λ-MnO_2, $LiMn_2O_4$, $Li_{1+x}Mn_{2-x}O_4$, $Li_2Mn_2O_4$, Li_2MnO_3, $Li_2Mn_4O_9$ and $Li_4Mn_5O_{12}$. These involve Mn^{3+}, Mn^{4+} or an average valence state somewhere in between; they are summarized in Table 4.1. The structures in the Li_2MnO_3-$LiMnO_2$-λ-MnO_2 part of the phase-diagram are either spinel or rock-salt related. There are also substituted phases like $Li_{1+x}Mn_{2-x}O_4$ ($0 \leq x \leq 0.33$), where extra Li occupies the Mn site, which may stabilize the structure by raising the average valence number.

Table 4.1 A summary of Li-Mn-O phases relevant to this thesis. [49,50]

Composition	Spinel notation	Mn valency	Chrystallographic structure (a, b, c in Å)
λ-MnO_2	$(\square_{1.0})[Mn_2]O_4$	4.00	Cubic spinel (Fd3m) a = 8.067
$LiMn_2O_4$	$Li[Mn_2]O_4$	3.50	Cubic spinel (Fd3m) a = 8.2476(2)
$Li_{1+x}Mn_{2-x}O_4$	$(Li_{1.0})[Li_xMn_{2-x}]O_4$	3.50-4.00	Cubic spinel (Fd3m) a ≅ 8.21-8.24
$Li_2Mn_2O_4$	Rock-salt	3.00	Tetragonal rock-salt ($I4_1/amd$) a = 5.662(2); c = 9.274(4)
Li_2MnO_3	Rock-salt	4.00	Monoclinic rock-salt (C2/m) a = 4.937(1); b = 8.532(1); c = 5.03(2)
$Li_2Mn_4O_9$	$(Li_{0.89}\square_{0.11})[Mn_{1.78}\square_{0.22}]O_4$	4.00	Cubic spinel (Fd3m) a = 8.162
$Li_4Mn_5O_{12}$	$Li[Li_{0.33}Mn_{1.67}]O_4$	4.00	Cubic spinel (Fd3m) a = 8.1616(5)

In the $LiMn_2O_4$ spinel structure (space-group: Fd3m), a cubic close-packed (ccp) array of oxygen ions occupy the 32e position, Mn ions are located in the 16d site, and Li in the 8a site. The Mn ions have an octahedral coordination to the oxygens, and the MnO_6 octahedra share edges in a three-dimensional host for the Li guest ions (Fig. 4.2). The 8a tetrahedral site is situated furthest away from the 16d site of all the interstitial tetrahedra (8a, 8b and 48f) and octahedra (16c). Each of the 8a-tetrahedron faces is shared with an adjacent, vacant 16c site. This combination of structural features in the stoichiometric spinel compound constitutes a very stable structure.

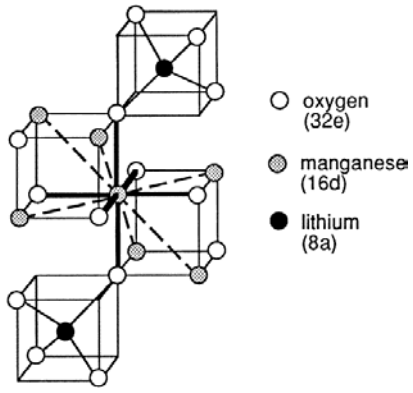

Figure 4.2 Part of the unit cell of $LiMn_2O_4$ showing the local structure around octahedrally coordinated manganese in an ideal spinel lattice. Mn-O bonds are represented by heavy solid lines; linear chains of manganese ions in neighboring edge-sharing octahedra are indicated by dashed lines.

4.2 Lithium extraction/insertion mechanism

The compound $LiMn_2O_4$ is a stable phase in the middle of the discharge curve of λ-MnO_2. [51] On further reduction, the material converts into $Li_2Mn_2O_4$. [52] The phases and phase transitions during reduction from λ-MnO_2 to $LiMn_2O_4$ have been the focus of debate in many publications (**paper IV**). [53-57] From $LiMn_2O_4$ to $Li_2Mn_2O_4$, there is a distinct first order phase transition. The focus of this thesis has been on the 4V region.

When Li ions are inserted into the spinel host structure, they occupy the octahedral 16c sites. Since this site is face-sharing with the 8a tetrahedra, the Li ions in the tetrahedral site are instantly displaced into the vacant 16c site, causing a first-order phase transition. When the Mn^{3+} (d^4) concentration increases, a Jahn-Teller (JT) distortion also occurs with a gain in energy equal to ε (Fig. 4.3). The crystal symmetry decreases from cubic (c/a = 1.0) to tetragonal (c/a ~ 1.16); this imposes a large strain on the individual spinel particles, that ultimately results in electromechanical grinding; the reversibility of this phase transition is poor. However, it has been shown in recent studies that significant strain effects and nano-sized regions are introduced into the $LiMn_2O_4$ material by ball-milling and possibly partial oxidation, resulting in a good utilization of the material on Li insertion to $Li_2Mn_2O_4$. [58] There has also been some effort to develop a layered $LiMn_2O_4$ material to better utilize the full discharge capacity. [59]

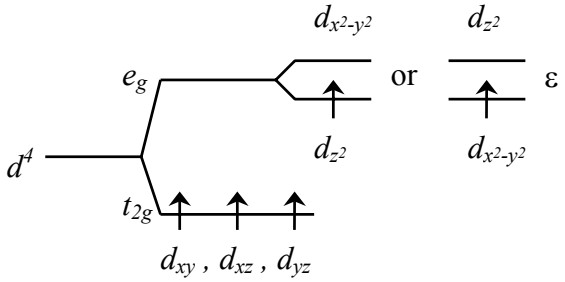

Figure 4.3 Schematic representation of the splitting of the Mn 3d orbital in Mn^{3+} (d^4).

The situation is quite different during the removal of Li from the $LiMn_2O_4$ structure; the unit cell volume decreases gradually and isotropically as the Li-ion concentration decreases. The removal of Li from $LiMn_2O_4$ occurs through a two-step reaction around 4V; two potential plateaus can be discerned in the charge curve, separated by 100-150 mV. Rigorous studies have also shown that the material goes through at least one two-phase region during charge/discharge. [53,54] The structure of these intermediate phases are not yet determined, but single-crystal studies have shown that superstructures may occur in the upper part of the potential curve. [60] An ordered $Li_{0.5}Mn_2O_4$ phase has been proposed to correspond to the step in the potential curve, [61] but neutron studies showed no evidence for this. [54]

4.3 Problems and solutions

We see then that $LiMn_2O_4$ is, in principle, an excellent candidate as a cathode material in secondary Li-batteries. The theoretical capacity is competitive with existing materials and the 3-D host network should function well in the 4V region. However, there are some problems with the material that leads to a slow capacity loss and need to be solved; they will be reviewed in this section.

Several processes has been proposed as source of the room-temperature capacity fade in $LiMn_2O_4$:

1. Loss of Mn through disproportionation of trivalent Mn. Hunter discovered this already in 1981, [62] and proposed a disproportionation reaction:

$$2\ Mn^{3+}_{(solid)} \longrightarrow Mn^{4+}_{(solid)} + Mn^{2+}_{(solution)} \qquad (5)$$

   This reaction is dependent on the acidity of the electrolyte; the choice of solvent and salt is also important from this point of view. Jang and Oh report the amounts of solvent-derived acid and dissolved Mn as a function of storage time in different electrolyte systems. [33] They find that the extent of spinel dissolution is salt-dependent in the following decreasing order:

$$LiCF_3SO_3 > LiPF_6 > LiClO_4 > LiAsF_6 > LiBF_4$$

   The dissolution of divalent Mn will not only cause a loss of active cathode material but also affect the anode. Solvated Mn^{2+} will be transported through the electrolyte and ultimately plate onto the anode. This will deplete the Li content in the anode, since the reduction of Mn will oxidize Li from the anode:

$$Mn^{2+} + 2\ LiC_6 \longrightarrow Mn + 2\ Li^+ + \text{graphite} \qquad (6)$$

2. Formation of a Li-rich surface on cycling – leading to a JT transformation to the tetragonal $Li_2Mn_2O_4$ phase and ultimately to Li_2MnO_3 by dissolution of MnO – was proposed by Thackeray and co-workers as a variation of mechanism 1. [63,64] The electrode would incorporate extra Li in the outermost surface layer, through the over-potential driving the electrochemical reaction during cycling. Mn^{2+} is known to dissolve from the active electrode, here as MnO. On prolonged cycling, the combined effects of overcharge and dissolution transforms a significant amount of the electrode into Li_2MnO_3; this phase was detected by XRD measurements. (crossref. Cho) The final reaction is:

$$Li_2Mn_2O_4 \longrightarrow Li_2MnO_3 + MnO \qquad (7)$$

3. Instability of the de-lithiated λ-MnO_2 phase [65] and self-discharge or loss of oxygen from the host structure, coupled to solvent oxidation in the high-voltage region. [4,66]

4. Structural degradation during cycling over the high-voltage two-phase region (approx. $Li_{0.5}Mn_2O_4$ - λ-MnO_2). [55]

A solution to the room-temperature capacity fade problem is cation substitution. Solid solutions in which monovalent, divalent or trivalent cations substitute the Mn cation increase the average Mn oxidation state. This results in a reduction of the unstable Mn^{3+} cations and a material less susceptible to the disproportionation reaction. [48,67,68] Substitution of Al, for example, also decreases the cell parameter of the pristine material; an important factor for a well-functioning spinel electrode. [69] Al doping has also been shown to improve the layered 2D cathode materials. [70] Anionic doping is another way of improving the Mn spinel material. [71]

At slightly elevated temperatures (ET), the capacity fade in Mn spinel electrodes escalates. This is a problem that must be solved since the applications for Li-ion batteries contain electronic circuits that generates heat, *e.g.* cell-phones and lap-tops.

Tarascon and co-workers have performed a thorough study of the ET problem. [45,69,72-74] They conclude that the mechanisms responsible for this capacity fade are the same at ET's as at room-temperature. [69] Evidence was presented for a failure mechanism originating in the lithiated state, and the cell parameter of the pristine material was found to be a crucial factor.

The difficulties associated with the Mn spinel at ET can be connected with the presence of HF acids in the electrolyte, which causes a significant quantity of Mn dissolution. The surface area of the material can be related directly to capacity fade, as an increased surface area also increases the area of electrolyte contact and thus the HF attack on the material. The surface area is also important for obtaining a good rate-capability as smaller grains, *i.e.* a larger surface area, will facilitate faster lithiation/de-lithiation.

A significant proton exchange at ET has been proposed for $Li_{1+x}Mn_{2-x}O_4$ where $x \geq 0.05$. [45] The Mn spinel does not here follow Hunter's disproportionation reaction, as shown by acid treatment of the material, [75,76] but rather a proton exchange where the protons occupy the 96g-site in the spinel framework. [77]

A material with a smaller cell parameter was synthesised with Al cation doping as a solution to the elevated temperature problem; its capacity was further improved by F anion doping. [69]

Another focus for possible improvement is the interface region, and attempts have been made to pre-fabricate a protective surface coating. [73] This works well in early cycles, but does not improve prolonged cycling. By introducing small amounts of inorganic compounds into the electrolyte, it is possible to improve the capacity retention of Li-ion batteries, probably by reaction of the additives with HF in the electrolyte and hence lowering the HF concentration. [78] Coating the cathode particles with Li_2CO_3 lower the acidity of the system, [79] while coating with Al_2O_3 has improved the stability of Li-Mn-O compounds. [80]

5. EXPERIMENTAL

"Anger is a gift"

- Rage Against the Machine

5.1 Materials characterization

The electrochemical and structural properties of the cathode material depend largely on the initial spinel composition. [53,54,56,57,72] In this work, a well characterized commercial $LiMn_2O_4$ powder was therefore used in all studies to minimize any possible effects of synthesis. Electrodes from the same preparation batch were used in analytical measurements where the electrode morphology can be a decisive factor, *e.g.* reflectance IR.

Inductively coupled plasma (ICP) analysis was used to determine the composition of the material to $Li_{1.02}Mn_{1.98}O_4$. Neutron diffraction (ND) was used to confirm this composition, but the differences between a stoichiometric $LiMn_2O_4$ and a substituted $Li_{1+x}Mn_{2-x}O_4$ material with $x \leq 0.05$ proved to small to be determined by Rietveld analysis.

The surface area of the pristine material was determined to 3.0 m^2/g, and 4.5 m^2/g after ball-milling.

The particle size distribution was measured by Low angle laser light scattering (LALLS), showing the pristine material to have an average grain-size diameter of ~28 μm. After 30 min of ball-milling, the average grain size decreases to ~8.0 μm; additional milling did not change the size further.

5.2 Electrode and battery preparation

Composite $LiMn_2O_4$ electrodes were made by extrusion of a slurry comprising 80 wt% $LiMn_2O_4$ (Selectipur®, Merck), 15 wt% Shewinigan Black carbon powder and 5 wt% ethylene propylene diene terpolymer (EPDM) binder dissolved in cyclohexane onto an aluminium foil. All electrochemical cycling was performed using flat and flexible laminate cells, consisting of aluminium discs (diameter = 20mm) coated with the $LiMn_2O_4$ /carbon black/EPDM composite electrode paste as working electrode, a glass-wool separator soaked in electrolyte, and a lithium-metal counter electrode. These components were vacuum-sealed into a polymer-coated aluminium envelope. Preparation and assembly were carried out in argon atmosphere in a glove-box (<2ppm O_2/H_2O). The electrolyte was 1M salt in an EC/DMC 2:1 by volume mixture. Two salts were used: $LiPF_6$ (Selectipur®, Merck) and $LiBF_4$ (battery grade, Tomiyama). The

solvents were used *as received*, while the salts were dried under vacuum at 80°C and 120°C, respectively, prior to use.

The *in situ* 3-electrode cells (**paper IV**) consist of circular perforated aluminium disc (diameter = 20 mm) coated with the $LiMn_2O_4$/carbon black/EPDM composite electrode as working electrode, a Solupor® (DMS Solutech) separator soaked in electrolyte, and a lithium-metal counter electrode. Another separator soaked in electrolyte was placed on the backside of the perforated Al current collector, together with a small piece of lithium pressed onto on a Ni strip, used as reference electrode. In this way, the potential of the studied electrode can be measured and controlled, and the ohmic contribution (iR-drop) to the electrochemical response minimised by the position of the reference electrode. The stack was vacuum-sealed into a polymer-coated aluminium envelope.

5.3 X-ray diffraction

Constructive interference of X-ray radiation occurs in a material when Bragg's law is satisfied:

$$2d \sin\theta = n\lambda \tag{8}$$

Where d is the distance between equivalent atomic planes, θ is the angle between the incident beam and these planes, n is an integer and λ is the wavelength. The scattered intensity can be measured as a function of scattering angle 2θ. Analysis of the resulting X-ray diffraction (XRD) pattern is an efficient method for determining the different phases present in the sample. Since the wavelength of X-rays used is of the same order of magnitude as the interatomic distances and bond lengths in crystalline solids (~1 Å), the XRD method serves well to determine the structure of crystalline materials.

The cubic structure of the $LiMn_2O_4$ material studied in this thesis facilitates the determination of the lattice parameter (a_c) from one diffraction peak according to:

$$\frac{1}{d} = \frac{\sqrt{h^2 + k^2 + l^2}}{a_c} \tag{9}$$

Where d is the spacing of the crystal planes and h, k, l are the Miller indices of the measured reflection.

The study of ion-insertion processes in electrode materials has been shown to be particularly amenable to *in situ* X-ray diffraction (XRD) methodology. Its advantage lies in its ability to monitor structural changes in the electrode material as ion insertion or de-insertion proceeds. This, combined with simultaneous electrochemical measurements, provides valuable information inaccessible to *ex situ* experiments on the relationship between structure and electrochemical properties. This has been shown in many studies of $LiMn_2O_4$ [56,72,81-83] as well as other cathode ($LiNiO_2$, [84] $LiCoO_2$ [85]) and anode materials. [86,87]

The use of flat Li-ion cells in transmission mode has proved particularly convenient for *in situ* XRD studies of electrode materials. The use of reflection mode can limit the statistics of the data collected, as there will be a larger contribution from the surface region at lower 2θ angles. An experimental set-up where the entire bulk material is probed simultaneously is preferred.

5.4 Photoelectron spectroscopy [88,89]

Surface analysis by X-ray Photoelectron Spectroscopy (XPS) is accomplished by irradiating a sample with monochromatic X-rays under ultra-high vacuum and analysing the energies of the emitted electrons. The photons have a penetrating power of the order of 1-10 μm in a solid sample. These interact with atoms in the surface region by the photoelectric effect (Fig. 5.1) and cause core electrons to be emitted. The kinetic energy (E_k) of the emitted core electrons is given by Eq. 10:

$$E_k = h\nu - E_b - \phi_s \tag{10}$$

where $h\nu$ is the energy of the photon, E_b is the binding energy of the atomic orbital from which the electron originates, and ϕ_s is the spectrometer work function. The binding energy of a core electron is conceptually (but not strictly) equivalent to the ionisation energy of that electron, and is characteristic of the individual atom to which it is bound. Since there is a variety of possible ions for each atom-type, there is a corresponding range of kinetic energies in the emitted electrons. This facilitates qualitative elemental analysis. The binding energy of the core-level of an atom is affected by its chemical environment; the shifts in binding energy give information as to the local environment and its oxidation state. Chemical shifts arise from the variation of electrostatic screening experienced by core electrons as valence electrons are drawn towards or away from the atom of interest.

Due to the interaction of electrons with matter, the path length of the electron is of the order of tens of Ångströms (Å). While ionisation occurs to a depth of a few micrometers, only the electrons within tens of Å below the surface can thus leave the surface without energy loss. The electrons that undergo energy-loss processes (*e.g.* inelastic scattering) form the background, while the electrons that escape without energy loss give the peaks of interest in the spectra.

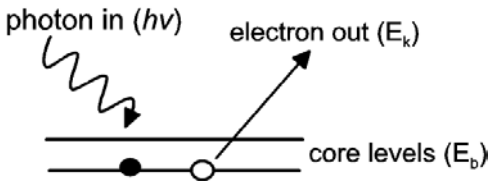

Figure 5.1 The photoelectric effect.

The quantitative determination of the atomic fraction of a specific element (C_x) can be expressed by the generalized formula:

$$C_x = \frac{n_x}{\sum_i n_i} = \frac{I_x / S_x}{\sum_i I_i / S_i} \tag{11}$$

where S is the atomic sensitivity factor, a factor dependent on the element and the instrumental set-up; n is the number of atoms of the element per cm^3 of the sample; I is the number of photoelectrons per second in a specific spectral peak.

5.5 Infra-red spectroscopy [90]

Fourier-transformed infrared (FT-IR) spectroscopy can be used to detect changes in coordination and configuration of molecular species in a system. The vibrations of individual bonds or groups in a molecule have the same frequency as electromagnetic radiation in the IR region. If the dipole moment of the molecule changes when it vibrates, it is IR-active and the radiation is absorbed by the molecule. This absorption excites the molecule from its ground state (v = 0) to a higher vibrational state (v = 1) and the difference in energy between the two states (E_0) is related to the position of the vibrational band in the spectrum. The vibrations can be caused by stretching, scissoring, rocking or wagging of individual groups, and the presence or absence of such modes makes it possible to distinguish between different coordination situations in the samples. The intensity of a band is related to the population of a certain vibrational state, the change in molecular dipole moment and the number of molecules vibrating at that frequency. FT-IR is an efficient tool for the identification of organic compounds, which generally provide numerous peaks in the mid-infrared region.

5.6 Thermal analysis [91]

The thermal analysis technique used in this thesis work has been Differential Scanning Calorimetry (DSC). This determines the energy (enthalpy) changes in a sample, which is accomplished by heating (or cooling) a sample and a reference at a preset rate, and measuring the compensating heat-flux that maintains the sample temperature within preset limits. The experimental DSC curves plot the heat-flux (mJ/s) or the specific heat capacity Cp (J/gK) against temperature. The compensating heat-flux is directly proportional to the change in internal energy (enthalpy) of the sample.

6. SURFACE CHEMISTRY OF $LiMn_2O_4$

"Even flow, thoughts arrive like butterflies…"

- Pearl Jam

6.1 Electrode/electrolyte interface

Interfaces are the critical regions of an electrochemical device; it is vital that they are well characterized. An intermediate migration-step through a surface film has been found on all the commonly used Li-ion battery materials by impedance measurements. [43,44,92] Whether this surface film is produced by processes associated with cell-cycling or has a chemical origin is of fundamental interest in understanding the cathode/electrolyte interface. A study was initiated to answer to this question and to investigate the nature of the species formed on the electrode surface during both cycling and storage in electrolyte (**paper I**). [93] We chose the most commonly used solvent system and the two most promising electrolyte salts. We monitor the different environmental states for these model-systems.

In Fig. 6.1, we see the typical appearance of an XPS spectrum of the surface of an electrode cycled in EC/DMC $LiPF_6$ electrolyte. The F1s peak is mainly from LiF, but there is also a contribution from a Li_xPF_y compound. Mn2p has a rather low signal, due to the coverage of the inorganic/organic surface film and the surface Mn valence state could not be determined from these measurements; this was later done in a special study (**paper II**, 6.2). The O1s spectrum has a sharp feature around 529.5 eV from the $LiMn_2O_4$ oxygen, and two bands associated with the surface film. Around 533 eV, there is a strong band originating from both organic and inorganic compounds. It belongs partly to a poly(oxyethylene) [94-96] and partly to a phosphorous compound. [88,97] At higher binding energy (BE), there is an oxygen band associated with a C1s band at 290 eV, most likely from solvent residues. C1s have two major bands besides this small band at 290 eV. At 284.3 eV, there is a strong band from the nanocrystalline turbostratic graphitic regions in CB, but more interesting is the band at 285.5 eV (Fig. 6.2). This is a polymeric band, but at a slightly higher BE than is normally found in a $(CH_2CH_2)_n$ polymer (Scheme 3.1 f). It is most likely that there is some electronegative constituent attached to this polymer, and the 285.5 eV peak can thus be related to the O1s band at 533 eV. P2p reveals a broad feature with more than one P oxidation state. The higher BE band is from the Li_xPF_y compound and the lower from a phosphorous oxide compound. Li1s is dominated by the LiF contribution to the Li peak. See Table 6.1 for a summary of XPS peak assignments.

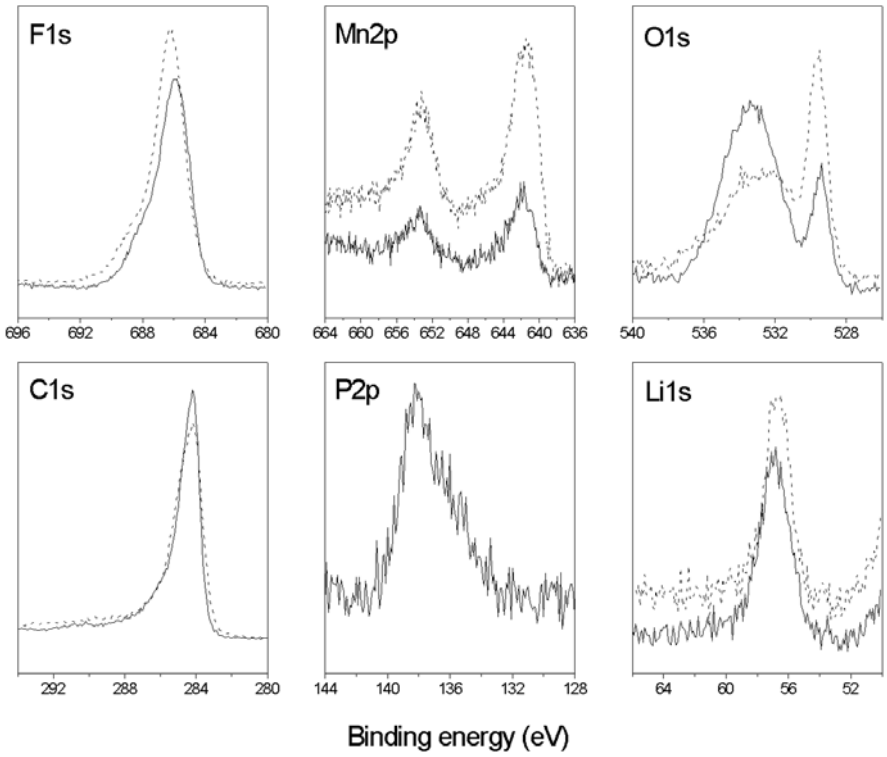

Figure 6.1 XPS spectra of an electrode after 50 cycles at C/3, $LiPF_6$ electrolyte. Solid line: before Ar-sputtering. Dotted line: 60 s Ar-sputtering.

The amount of surface material present increases with cycle number and storage time. This suggests that the layer formed on the $LiMn_2O_4$ cathode is not dense enough to serve as a sufficient barrier between electrolyte and the oxidising environment close to the cathode surface. Fresh electrolyte is transported to the electrode surface and oxidation continues with time. This is in contrast to the situation on the graphite anode, where the SEI layer formed during the first discharge covers the electrode surface so as to prevent further reduction of the electrolyte in subsequent cycles. The cathode surface layer could thus be termed **Solid Permeable Interface (SPI)** rather than an SEI, which implies a passivated surface. The cathode/electrolyte interface can limit cell performance by consuming electrolyte as cycling progresses. This can also be seen from cycling curves for $LiMn_2O_4$ cells, where the charge (Q) accumulated during the oxidation of $LiMn_2O_4$ is often greater than the charge accumulated in the reduction process, implying a side reaction in the cell, *e.g.* electrolyte oxidation (**paper I**). The formation of an organic compound closest to the surface, rather than an inorganic compound seems to limit the capability to passivate the electrode (**paper III**).

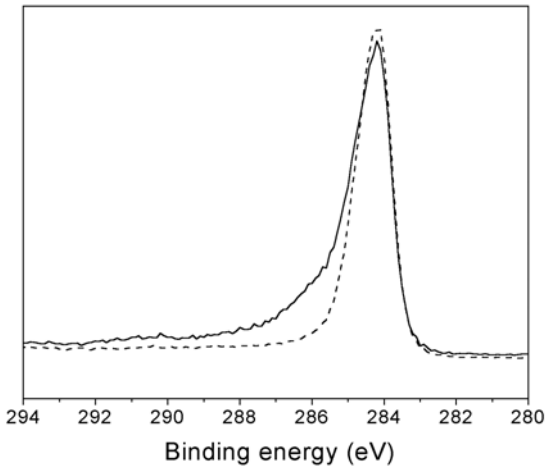

Figure 6.2 XPS C1s spectrum of a pristine electrode (dotted line) compared to after 50 cycles at C/3 (solid line), $LiPF_6$ electrolyte.

Comparison of an electrode stored for exactly the same period of time as another electrode is cycled, in this case 300h and 50 cycles at C/3, reveals an almost identical surface. The XPS depth profiles of the electrodes are displayed in Fig. 6.3; the relative amounts of the elements are almost identical in the two electrodes. A small increase in Li and F can be observed just below the surface, while the C content is decreasing. This indicates the existence of different layers in the surface film, where some species are formed closer to the electrode surface than others. As we move into the sample, the F, O, P and Li concentration decreases, while Mn and C increase as more of the bulk electrode is exposed.

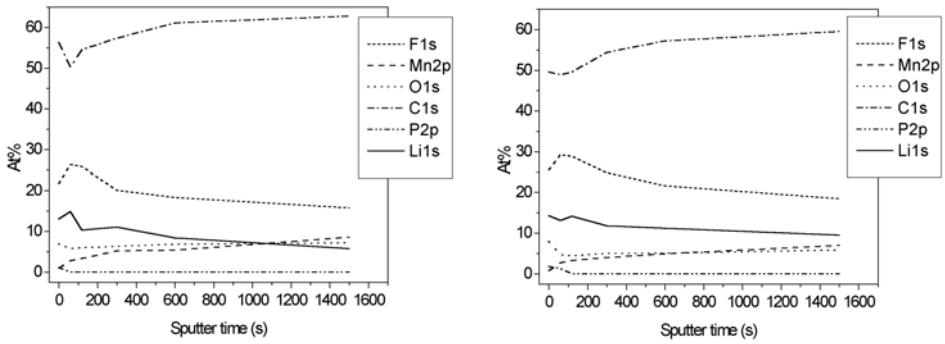

Figure 6.3 XPS depth profiles of electrodes in $LiPF_6$ electrolyte. A. 50 cycles at C/3. B. Stored 300h.

The influence of state-of-charge (SOC) on the surface film is somewhat surprising. One would expect that the surface film would grow thicker as the potential increases. The surface of an electrode stored for 300h at SOC 100% (4.3 V *vs.* Li/Li^+) was compared to an electrode stored at SOC 0% (3.4 V *vs.* Li/Li^+). The amount of surface species was found to be lower at the high-voltage electrode compared to the electrode stored at SOC 0%. This is in conflict with the expectations and can be due to a more complete oxidation of the solvents, resulting in gaseous end-products, *e.g.* CO_2.

When $LiBF_4$ was used as electrolyte salt, small additional C1s XPS bands were detected at roughly 287 and 289 eV. These are the ether- and carbonate- carbonyl-bands, respectively. This suggests a surface film with more organic products when $LiBF_4$ is used; in good agreement with the results at elevated temperature (**paper III**).

From FTIR measurements (**paper I**), we observe bands corresponding well with poly(oxyethylene) (Fig. 6.4 A). This can only be seen in cycled electrodes, suggesting that the polymer is slightly thicker on the cycled electrodes at room temperature. At elevated temperatures, the polymeric bands also occur in the stored sample (**paper III**). The kinetics of surface-film formation may be slightly improved when a larger transport of material takes place to and from the electrode, as in the case of cycled electrodes. Li_xPF_y or $Li_xPO_yF_z$ compounds are also detected, thus supporting the XPS results.

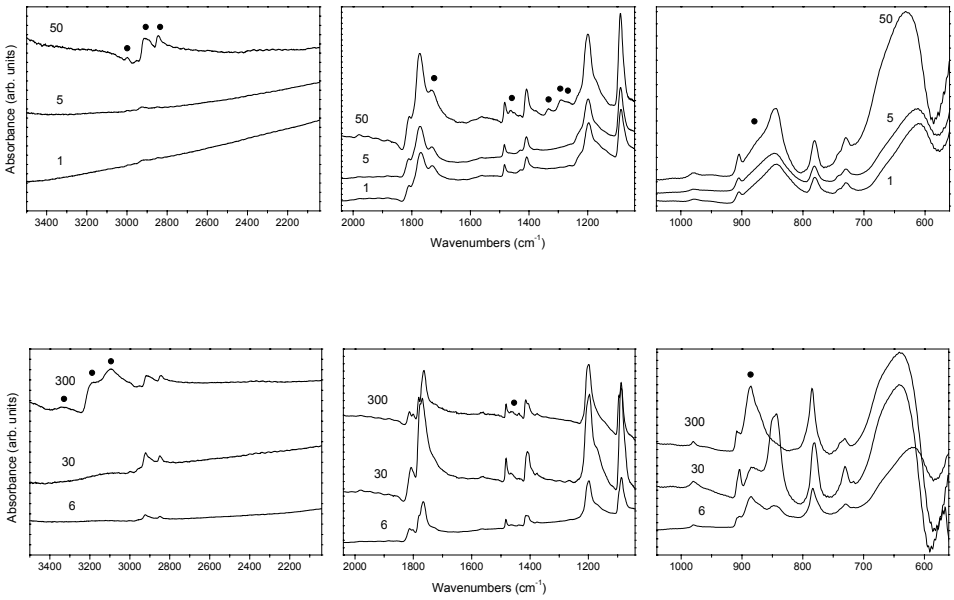

Figure 6.4 FTIR measurements on a series of electrodes. Dots indicate bands that are new compared to a reference. A. Cycled electrodes, number of cycles: 1, 5 and 50. B. Stored electrodes, times: 6, 30 and 300h.

Table 6.1 XPS peak assignments in elemental spectra from $LiMn_2O_4$ surfaces.

Surface component	C1s (eV)	O1s (eV)	F1s (eV)	P2p (eV)	B1s (eV)	$Mn2p_{3/2}$ (eV)	Li1s (eV)
C (graphite)	284.3						
C (amorphous)	284.8						
Polyether (PEO)	285.5	532.5-533.5					
$ROCO_2Li$	286-287	532-533					55
	290-291	534-535					
Li_2CO_3	290-291	531-532.5					55
Li_xPF_y			687-688	137-138			
P_2O_5		533.5		135.5			
		531.7					
LiF			685-686				56.5-57.0
Li_xBF_y			687-688		195		
$LiMn_2O_4$		529.5				642.0	
		531.5-532.0					

6.2 Electrode surface structure

A shift was observed in the Mn-O_6 octahedral band in the room-temperature FTIR measurements (Fig. 6.4). As storage and cycling progress, a shift occurs towards higher wavenumbers. A pristine electrode has a broad band at 610-620 cm^{-1} while, for the used electrodes, the band is shifted to 630-640 cm^{-1}. This shift has been interpreted as a Li-rich spinel-phase at the surface of the electrodes (**paper I**). [98] The shift can also be seen at elevated temperatures. A more thorough study of this band in the far-IR region resulted in an ambiguous interpretation of the band (**paper III**).

From DSC measurements (**paper III**) on electrodes at different SOC's, we observe that the temperature for the reactions between the active electrode material and the electrolyte increases as the Li-content increases in the sample; from 120°C for λ-MnO_2 to 150°C for $LiMn_2O_4$. The peak temperature is 160°C for an electrode cycled or stored at 60°C, indicating an even more lithiated sample (Fig. 6.5).

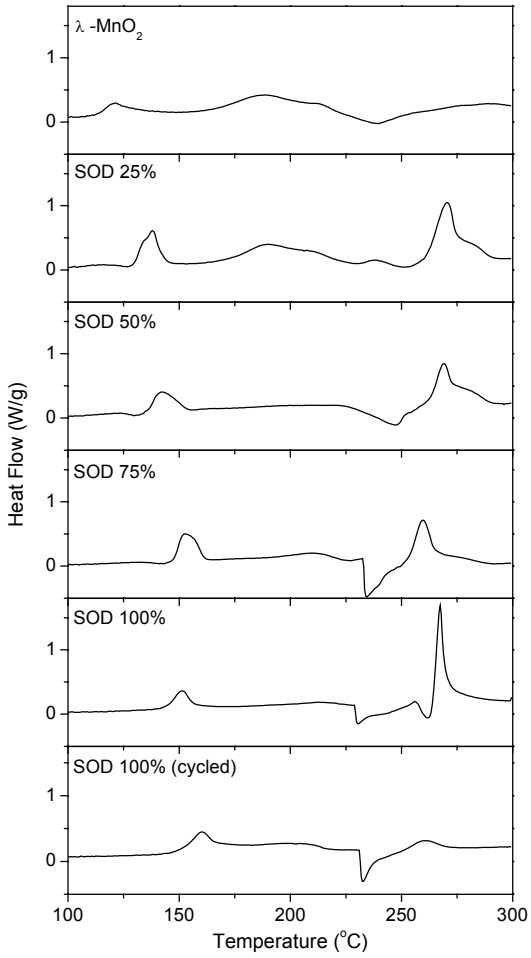

Figure 6.5 DSC measurements on a series of electrodes from cells stored at different SOC. Bottom measurement: DSC trace from an electrode cycled 50 times C/3. $LiPF_6$ electrolyte.

Structural analysis with XRD (**papers II and III**) show no new peaks for any cycled or stored samples, neither at room-temperature nor at 60°C (Fig. 6.6). The XRD phase analysis gives an average of the phase composition in the electrode and a thin surface layer is difficult to observe unless special XRD techniques are used, *i.e.* gracing incidence. It is thus better to use a more sensitive surface technique like XPS to monitor changes in the electrode surface structure.

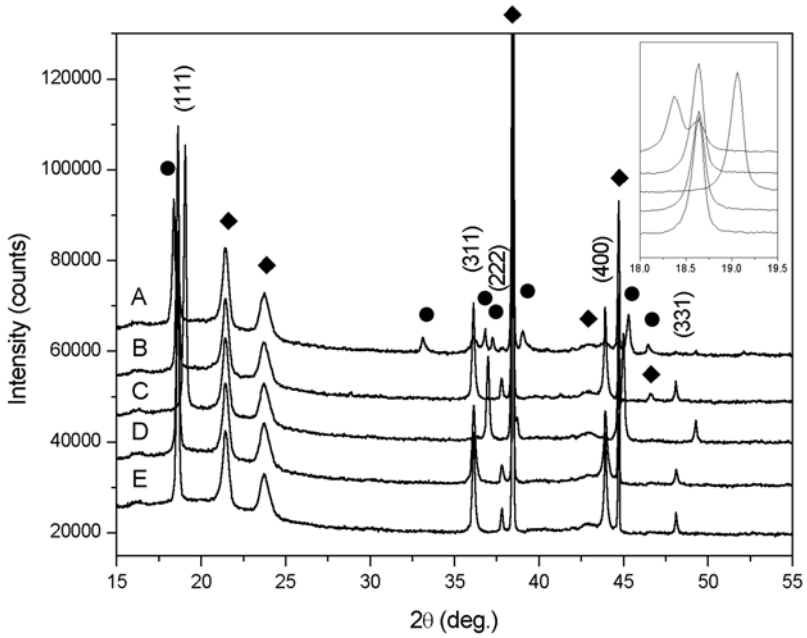

Figure 6.6 *Ex situ* XRD measurements on electrodes after cycling or storage at room-temperature. Dots are $Li_2Mn_2O_4$ reflections and diamonds are peak from the Al current collector or a protective laminate envelope. A. Discharged to 2.4 V. B. Pristine $LiMn_2O_4$. C. Charged to 4.3 V. D. Cycled 50 times at C/3. E. Stored 300h at OCP.

A thorough XPS investigation was performed on the same samples as in Fig. 6.6 (**paper II**). XPS on electrodes cycled or stored at elevated temperatures was unsuccessful due to the thick insoluble electrolyte-derived surface film on these samples (Ch. 6.3).

Although many XPS studies have been performed on different Mn-oxides, [99-106] there is a lack of XPS surface investigations for the $LiMn_2O_4$ system. Existing studies focus mainly on determining the valence state, or surface Li content using different synthesis approaches. [107-109] Mixed valence compounds, *e.g.* spinels, give a result that is a mix of the single-valence compounds, thus facilitating the determination of the Mn^{3+}/Mn^{4+} ratio.

The XRD measurements on reference samples of $Li_2Mn_2O_4$ (**paper II**) show that $LiMn_2O_4$ is still present and that phase-pure $Li_2Mn_2O_4$ is thus not obtained (Fig. 6.6). Despite this, the XPS results reveal a surface containing only Mn^{3+} (Fig. 6.7). Li seems to stay close to the surface, although the electrode was allowed to equilibrate before disassembly. The delithiated λ-MnO_2 reference could not be assigned to pure Mn^{4+} (Fig. 6.7) due to the Li remaining in the structure, giving a somewhat lithiated surface; it is generally accepted that about 20% of the Li is still present in the λ-MnO_2 phase. [53,110,111]

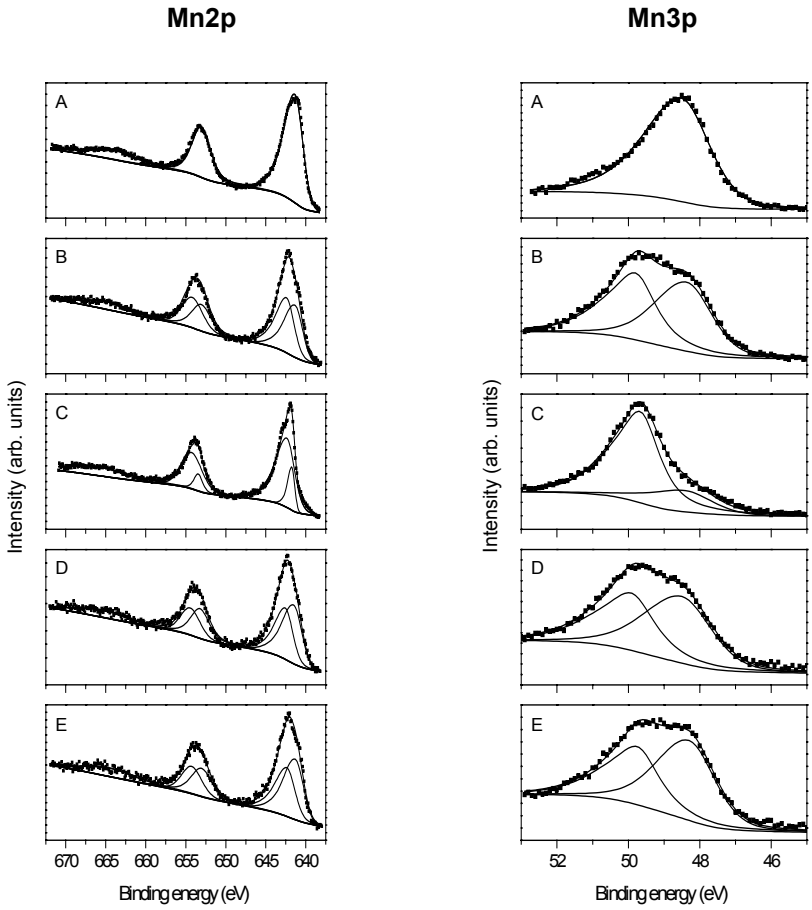

Figure 6.7 XPS Mn2p and Mn3p peaks from measurements on electrodes. A. Discharged to 2.4 V. B. Pristine LiMn2O4. C. Charged to 4.3 V. D. Cycled 50 times at C/3. E. Stored 300h at OCP. Solid lines represent each individual fitted peak and the total fit; the experimental data is presented by squares.

Analysis of the core-level spectra from the XPS measurements on cycled electrodes (**paper II**) shows an increase in the amount of Mn^{3+} (Table 6.2). This supports the literature results from TEM measurements where tetragonal $Li_2Mn_2O_4$ is found on the electrode surface after high-rate charge/discharge of electrodes. [63] Somewhat surprising, an even more reduced average valence-state is found on storage. The structures suggested as being formed on storage all have an average valence-state above 3.5. [45,74] The disproportionation process (described in 4.3) makes an Mn^{3+}-rich phase unstable, which will eventually decompose into a more stable Mn^{4+} compound and an Mn^{2+} compound soluble in the organic electrolyte. [62,64] From this study, it can be confirmed, however, that an Mn^{3+}-rich compound is formed as an intermediate step in the

decomposition of the $LiMn_2O_4$ material into an Mn^{4+} compound. The formation of a Li-rich Mn^{3+} compound progresses through the reduction of $LiMn_2O_4$, which promotes the oxidation of electrolyte (discussed in 6.4).

The Li-content increases significantly in the cycled and stored electrodes compared to a pristine electrode. It is, however, difficult to determine how much of the Li is associated with electrolyte-derived compounds, and how much that is present in the Mn-compound. Although the electrode has been thoroughly washed before analysis, the SPI is impossible to remove completely.

Table 6.2 Binding energies of core-level spectra (in eV).

	$Mn2p_{3/2}$	$Mn2p_{1/2}$ satellite	Mn3p	ΔE (Mn3s)	O1s	Mn^{3+}/Mn^{4+} $Mn2p_{3/2}$	Mn^{3+}/Mn^{4+} Mn3p
$Li_2Mn_2O_4$	641.4 (2.3)	664.2	48.5 (1.8)	4.96	529.5 (1.2)	–	–
	–		–				
$LiMn_2O_4$	641.4 (2.2)	665.2	48.4 (1.6)	5.63	529.4 (1.1)	0.91	0.99
	642.4 (2.2)		49.8 (1.4)				
λ-MnO_2	641.6 (1.0)	666.0	48.4 (1.8)	4.64	529.6 (1.0)	0.22	0.26
	642.4 (2.3)		49.7 (1.3)				
50 cycles C/3	641.5 (2.3)	665.5	48.5 (1.9)	5.24	529.7 (1.2)	1.19	1.16
	642.5 (2.2)		49.9 (1.6)				
Stored 300h	641.4 (2.4)	664.5	48.4 (1.7)	5.38	529.5 (1.1)	1.19	1.28
	642.4 (2.4)		49.9 (1.5)				

In parenthesis, full width at half maximum.

6.3 Elevated temperature effects

The effect of an increased temperature on the electrode/electrolyte interface is an important factor for the functionality and safety of an electrochemical battery system. This has earlier been investigated for the anode SEI; [112] we have here extended our studies to the cathode surface layer (**paper III**).

Additional C1s XPS peaks were observed in the stored and cycled elevated temperature samples (Fig. 6.8). These bands, at 286.8 and 288.8-289.4 eV, can be assigned to ether carbons and carbonate carbonyl carbons, respectively, originating from solvent decomposition products (Scheme 3.1). The EC and DMC products in Scheme 3.1a and 3.1g are commonly referred to as semi-carbonates. These have been found to give a carbonyl C1s peak shifted towards lower BE compared to Li-carbonate. [94,96] The instability of such semi-carbonates with temperature has been shown in the literature, [113,114] and it is unlikely that a stable semi-carbonate would be formed on the positive electrode surface at 60°C.

It is more likely that the shift in the C1s peak is caused by a distorted carbonate group with additional bonds to other organic groups. The most probable compound with these constituents is a polymerized carbonate [P1], which can be formed directly by polymerization of EC, initiated by EC oxidation. [44] The C1s peak indicating poly(oxyethylene)[P2] (described in 6.1) is also visible at 285-285.5 eV. Another possibility is the direct polymerization of EC initiated by strong Lewis acids, *e.g.* PF_5 and BF_3, into a poly(oxy-ethylene-*alt*-ethylene carbonate)[P1+P2] (Scheme 3.1 e). [40,115] These types of polymer have been shown to exist in the graphite SEI layer, especially at chemical lithiation and storage at elevated temperature. [112,116] From XPS measurements, it cannot be established definitively whether this is one [P1 + P2] or two separated polymers [P1] + [P2]; most likely it is a mixture of both.

Considerably more polymeric species are formed using $LiBF_4$ as electrolyte salt (Fig. 6.8 F) than with $LiPF_6$, possibly because BF_3 is a stronger initiator of polymerization. After a thorough DMC wash, the polymeric feature at 285.3 eV is unaffected and the polymerized carbonate peaks at 286.8 eV and 288.8 - 289.4 eV are still clearly present (Fig. 6.8 G).

The low BE O1s peak around 533 eV is dominant on electrodes cycled or stored at 60°C, although it decreases somewhat in intensity on thorough DMC washing (Fig. 6.9 C-G). This can be related to the large amount of P in the surface film and the formation of a phosphorous oxide compound. Poly-carbonate/poly(oxyethylene) peaks appear at 532-533 eV and 534-534.5 eV; the ether band is thus partly masked by the phosphorous oxide peak.

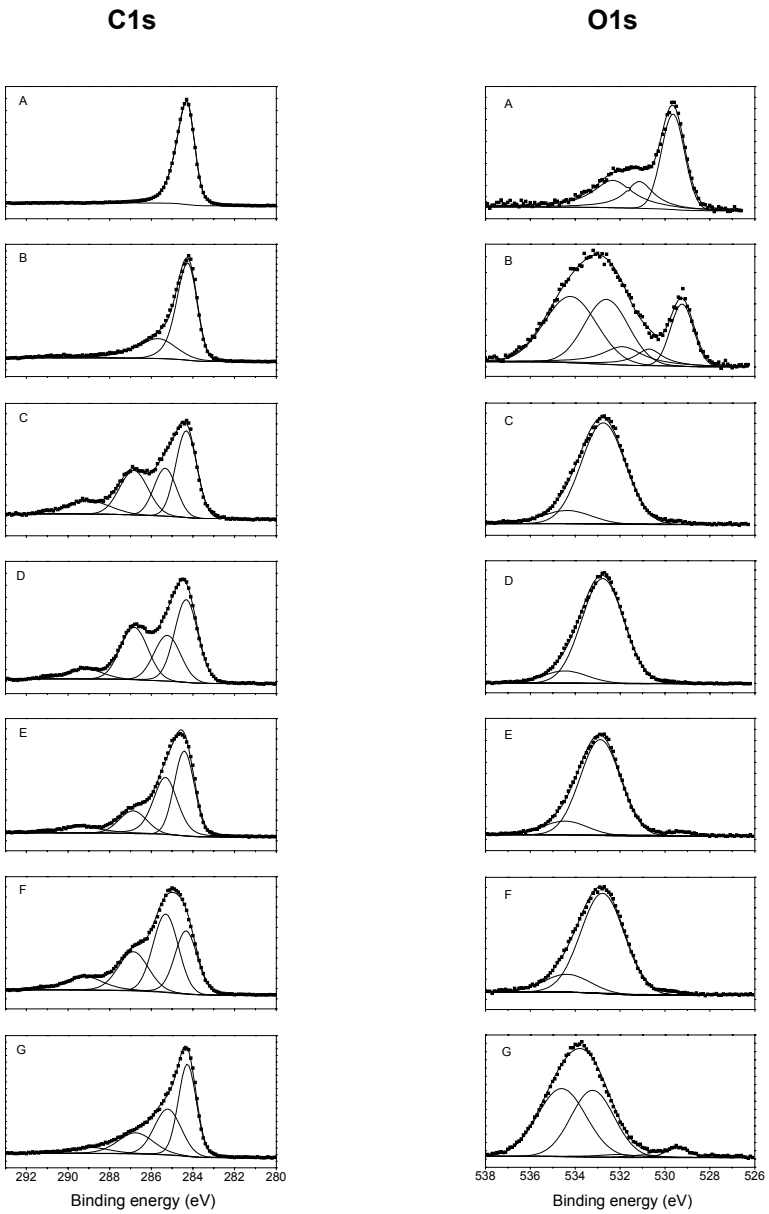

Figure 6.8 and 6.9 XPS C1s and O1s measurements on electrodes. A. Pristine electrode. B. Cycled 50 times C/3 at ambient temperature, $LiPF_6$ electrolyte. C. Cycled 50 times C/3 at 60°C, $LiPF_6$ electrolyte. D. Stored 300h at 60°C, SOD 100%, $LiPF_6$ electrolyte. E. Stored 300h at 60°C, SOD 0%, $LiPF_6$ electrolyte. F. Cycled 50 times C/3 at 60°C, $LiBF_4$ electrolyte. G. Stored 300h at 60°C, SOD 100%, $LiPF_6$ electrolyte, washed with DMC.

The P2p spectrum for a sample cycled at ambient temperature has a band at 138 eV from Li_xPF_y, and a shoulder at 135.4 eV assigned to a phosphorous oxide compound, *e.g.* P_2O_5 (Fig. 6.10 B). [88,97] After cycling or storage at 60°C, the 138 eV peak disappears and a new peak appears at 136.5 eV (Fig. 6.10 C-F). This new peak can be related to an increase in F-containing compounds (686-688 eV) and reflect the increase in $Li_xPO_yF_z$ compounds rather than the Li_xPF_y compounds present on ambient-temperature samples.

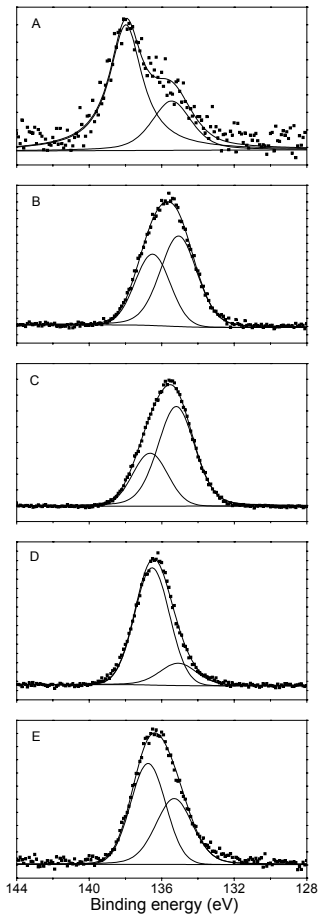

Figure 6.10 XPS P2p spectra of $LiMn_2O_4$ electrode surfaces. A. Cycled 50 times C/3 at ambient temperature, $LiPF_6$ electrolyte. B. Cycled 50 times C/3 at 60°C, $LiPF_6$ electrolyte. C. Stored 300h at 60°C, SOD 100%, $LiPF_6$ electrolyte. D. Stored 300h at 60°C, SOD 0%, $LiPF_6$ electrolyte. E. Stored 300h at 60°C, SOD 100%, $LiPF_6$ electrolyte, washed with DMC.

There is a strong contribution from the 135.1-135.3 eV peak on the electrodes cycled or stored at SOD 100% at 60°C (Fig. 6.10 B, C, E), while it is less prominent on the stored SOD 0% 60°C sample (Fig. 6.10 D). This peak coincides well with P_2O_5, together with the broad oxygen band at 533 eV. [97] The broadness of the oxygen band may thus be explained by the fact that two adjacent oxygen bands are associated with P_2O_5, non-bridging (P O bonds) and bridging oxygen (P-O-P bonds). The amount of the P2p P_2O_5 peak decreases somewhat after a thorough DMC wash (Fig. 6.10 E), coinciding with the decrease in the O1s P_2O_5 peak (Fig. 6.9 G), but there is still a substantial amount of both phosphorous compounds on the electrode after washing.

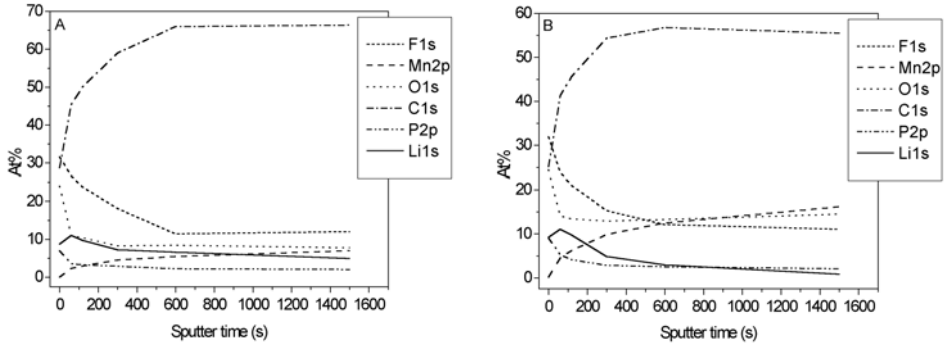

Figure 6.11 XPS elemental depth profile of $LiMn_2O_4$ electrodes. A. Cycled 50 times C/3 at 60°C, $LiPF_6$ electrolyte. B. Stored 300h at 60°C, SOD 100%, $LiPF_6$ electrolyte.

There is a striking resemblance in surface chemistry between an electrode cycled 50 times at C/3 in 60°C and an electrode stored for 300h at 60°C, as seen from the XPS data. A depth profile also reveals similar amounts of the elements regardless of cell history (Fig. 6.11). The influence of electrochemical cycling on surface film formation is thus minimal both at elevated and ambient temperature (6.1).

A comparison of the elemental compositions at the surface for each sample was made to get a picture of the different layers of the SPI film (Table 6.3). It is evident that there is a large amount of O, P, F, and Li compared to the other samples (O and P especially) during cycling or storage at SOD 100%, 60°C. Some of the P-O products can be removed through thorough washing with DMC, and a surface containing more of the polymeric carbon species is revealed. In the case of storage at SOD 0% (λ-MnO_2), the P-O products are less pronounced and, instead, more carbon products can be observed. The same goes for the electrode cycled in $LiBF_4$ electrolyte, which is similar in elemental composition to the stored λ-MnO_2 electrode (with B instead of P compounds). The lower amounts of boron compounds compared to phosphorous oxides can be explained by the higher instability of the $LiPF_6$ salt, making it more sensitive to impurities in the electrolyte. The Li concentration increases after washing (or sputtering), indicating that a Li-rich layer is present under the outer P-O layer, where LiF is the most likely product.

Table 6.3 Atomic percentage (at%) of elements on the surface of the electrode samples, EC/DMC 2:1 1M $LiPF_6$ or $LiBF_4$. The carbon content given in parentheses is the value after subtraction of the contribution from graphite, *i.e.* only surface-film carbon.

Electrode sample	Element						
	C1s	O1s	P2p	B1s	F1s	Li1s	Mn2p
$LiMn_2O_4$, 50 cycles, C/3, 60°C, $LiPF_6$	29.1 (17.8)	22.6	7.6		30.5	9.9	0.3
$LiMn_2O_4$, 300h storage, 60°C, $LiPF_6$	25.6 (15.4)	24.1	9.3		31.5	9.3	0.2
λ-MnO_2, 300h storage, 60°C, $LiPF_6$	46.3 (30.6)	18.0	5.1		23.8	6.5	0.3
$LiMn_2O_4$, 300h storage, 60°C, $LiPF_6$, washed	42.9 (24.6)	11.8	3.1		22.8	19.1	0.3
$LiMn_2O_4$, 50 cycles, C/3, 60°C, $LiBF_4$	52.0 (37.3)	19.9		5.3	16.4	6.2	0.2
$LiMn_2O_4$, 50 cycles, C/3, RT, $LiPF_6$	55.3 (18.2)	5.7	1.0		20.9	16.2	0.9
$LiMn_2O_4$ pristine	90.3	6.4				0.6	2.7

The Mn signal is barely detectable in the 60°C samples. Washing does not improve the Mn signal; the polymeric/polycarbonate species are too efficient in their coverage of the surface. All things considered, it could thus be concluded that the surface-film thickness increases as the temperature is increased. While the anode SEI layer seems to break down at a slightly elevated temperature and have to be reformed in the subsequent reduction cycle, [112] the cathodic surface layer increases in thickness with storage time, numbers of cycles and temperature.

The total reflectance FT-IR results support the XPS measurements with bands at 1167, 1270-1330, 1650, and 1730 cm^{-1} that can be assigned to polymeric species, polycarbonate or poly(oxyethylene) (Fig. 6.12, Table 6.4). [40,116,117] The 842 cm^{-1} ν(P-F) band is significantly broadened, with a shoulder at 870 cm^{-1} indicating new P-F compounds. The change of the 731 cm^{-1} band into a broad band with peaks at 716, 727 and 740 cm^{-1} can be caused by ν(P-O) from a phosphorous oxide compound. There are also bands at 930, 1175, 1270, 1393 and 1630 cm^{-1} assigned to $Li_xPO_yF_z$ and other phosphorous oxides (Fig. 6.13, Table 6.4). [116,118,119]

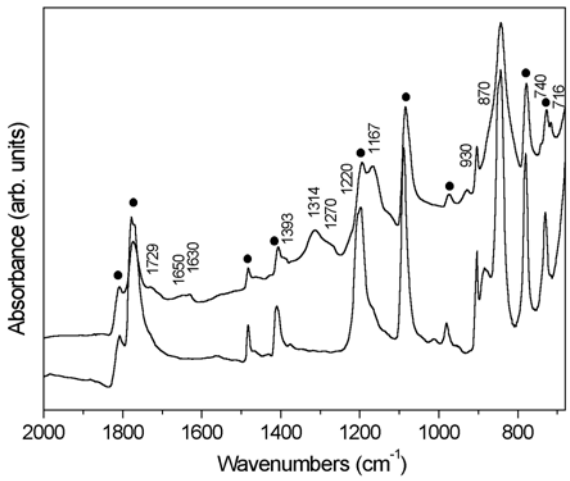

Figure 6.12 Total reflectance FT-IR measurement of $LiMn_2O_4$ electrode stored 300h at 60°C, SOD 100%, $LiPF_6$ electrolyte. 680-2000 cm^{-1}. Upper spectrum from the sample. Lower spectrum from electrolyte applied on a pristine electrode surface and measured. EC bands indicated by dots.

Table 6.4 Assignment of peaks in the IR spectra of $LiMn_2O_4$ samples cycled or stored in $LiPF_6$ electrolyte.

Frequency (cm^{-1})	Proposed assignment [a]
600-605	[Mn-O_6] $LiMn_2O_4$
615-620	[Mn-O_6] $LiMn_2O_4$
620-630	[Mn-O_6] $Li_{1+x}Mn_{2-y}O_4$
645	[Mn-O_6] $LiMn_2O_4$
740	P-O-P band P_xO_y
842	ν(P-F) Li_xPF_y
870sh	ν(P-F), ν(P-O) $Li_xPO_yF_z$
930	ν(P-F), ν(P-O) $Li_xPO_yF_z$ or P_xO_y
1167	ν(C-O-C)
1175	EC, $Li_xPO_yF_z$ or P_xO_y
1270	(CH_2)
1285	$Li_xPO_yF_z$ or P_xO_y
1314	$\nu(C=O)_s$
1287	(CH_2)
1332	(CH_2)
1393	(CH_3,CH_2) or P_xO_y
1630	Li_xPF_y or $Li_xPO_yF_z$
1650	$\nu(C=O)_{as}$
1729	ν(C=O)

[a] ν, stretching; sh, shoulder.

6.4 Mechanisms

A model for the SPI is proposed on the basis of **papers I-III**. Figure 6.13 gives a schematic picture of the SPI at elevated temperatures.

A layer of polymer/polycarbonate is formed closest to the active electrode-particle surface during cycling or storage at SOD 100%; a layer of LiF and an outermost region with $Li_xPO_yF_z$ and phosphorous oxides (or Li_xBF_y and boron oxides) precipitates on this layer (Table 6.3, Figs. 6.8-6.10). The dissolution of Mn from the spinel material occurs in the lithiated state, where the disproportionation of Mn^{3+} can progress (4.3); it can be described by Hunter's reaction: [62]

$$2\ LiMn_2O_4 \longrightarrow 3\ \lambda\text{-}MnO_2 + MnO + Li_2O \quad (12)$$

$$MnO + 2\ H^+ \longrightarrow Mn^{2+} + H_2O \quad (13)$$

Mn^{2+} forms complexes with the solvent molecules in the electrolyte and goes into solution. Li_2O from Eq. 12 can react directly with phosphorous compounds, formed from the decomposition of $LiPF_6$, [35] and form P_2O_5 according to:

$$LiPF_6 \longleftrightarrow LiF + PF_5 \quad (14)$$

$$PF_5 + H_2O \longrightarrow 2HF + POF_3 \quad (15)$$

$$2\ POF_3 + 3\ Li_2O \longrightarrow P_2O_5 + 6\ LiF \quad (16)$$

The formation of phosphorous oxides would thus be driven by the disproportionation of Mn^{3+}; this would explain the surplus of phosphorous oxides on the SOD 100% samples compared to the SOD 0% samples. It would also explain the increase in phosphorous oxides with temperature, since the dissolution of Mn will increase at elevated temperatures. [45]

Eqs. 12-15 constitutes a cycle, where H_2O is consumed in Eq. 15 and reformed in Eq. 13; HF drives Eq. 12 and 13 towards Mn^{2+} (sol.). In the $LiBF_4$ case, we get a smaller amount of boron oxide due to the higher stability of the salt.

It was seen from XPS that a stronger driving force exists for the formation of the polymer/polycarbonate compounds at SOD 0%than at SOD 100%. The initial potential is higher during storage at SOD 0%, and thus more oxidation of solvent would be expected. From V-t registration and *ex situ* XRD measurements, it was observed that electrodes stored at SOD 0% self-discharged back to SOD 100% spontaneously during storage at 60°C for 300h. Electrolyte oxidation has been coupled to insertion of Li into the host structure and the driving force for electrolyte (El.) oxidation should be stronger than when only small changes occur in the lithium content: [4]

$$\lambda\text{-}MnO_2 + x\ Li^+ + x\ El. \longrightarrow Li_xMn_2O_4 + x\ El.^+ \quad (17)$$

This electrolyte oxidation may well occur in the form of solvent polymerization. Another possibility is the oxidation of electrolyte coupled to a loss of oxygen from the spinel structure at the highly delithiated spinel surfaces: [66]

$$Li_yMn_2O_4 + 2\ \delta\ El. \longrightarrow Li_yMn_2O_{4-\delta} + \delta\ (oxidized\ El)_2O \quad (18)$$

This reaction was proposed to occur in parallel with mechanism (17).

Discussions regarding solvent polymerization have chiefly focused on reactions involving EC, since EC is more likely to be oxidized at the positive electrode. This is because EC has a much higher dielectric constant ($\varepsilon = 95.3$) than DMC ($\varepsilon = 3.12$), so that the PF_6^- (or BF_4^-) anions will be solvated preferentially by EC. On applying a positive potential, the concentration of anions - and with it the concentration of EC - will increase in the double layer at the positive electrode. [120] The strong electrostatic field close to the cathode surface will align the polar EC molecules and facilitate oxidation. Through its higher polarity, EC will also be the preferred target for electrophilic and nucleophilic attack by contaminants in the electrolyte solution.

The changes in the Mn-O_6 octahedra observed in the IR measurements for SOD 100% samples (**paper I and III**) was suggested to reflect the creation of a lithium-rich surface. This was supported by the DSC and XPS measurements (**paper II and III**). For this to also be in agreement with Mn disproportionation discussions, the product must be of $Li_{1+x}Mn_{2-y}O_4$ type, where $y < 2x$: [74]

$$LiMn_2O_4 + 3x\ Li^+ + x\ El \longrightarrow Li_{1+3x}Mn_{2-x}O_4 + x\ Mn^{2+} + x\ El^+ \quad (19)$$

This reaction cannot be seen by XRD and should occur only in the outermost layer of the $LiMn_2O_4$ particle. The Li insertion following this mechanism must be much weaker than that during self-discharge for the SOD 0% samples, giving less solvent-derived products at SOD 100%.

However, as we know from the Mn XPS measurements (**paper II**), there is an Mn^{3+}-rich surface on the electrodes and Eq. 19 will give an average valence state > 3.5. The Li-insertion reaction, without loss of Mn, may thus drive the electrolyte oxidation process even during storage in the lithiated state:

$$LiMn_2O_4 + x\ Li^+ + x\ El \longrightarrow Li_{1+x}Mn_2O_4 + x\ El^+ \quad (20)$$

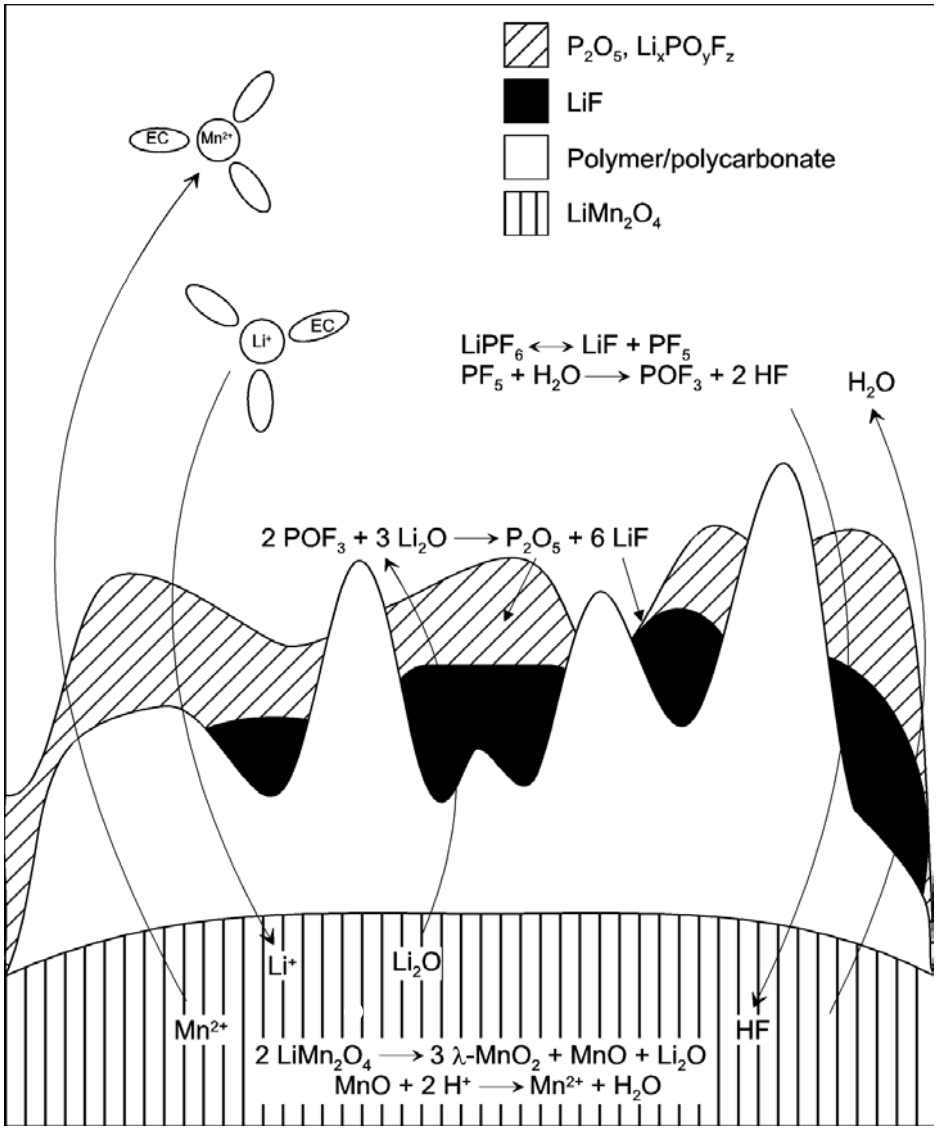

Figure 6.13 Model of the surface layer formed on a $LiMn_2O_4$ electrode.

7. KINETICS OF THE $LiMn_2O_4$ CATHODE

"Research: from the latin 'recircare' – to circle around repeatedly – "

7.1 Constant current

This study was aimed to investigate the factors limiting the kinetics of the $LiMn_2O_4$ cathode. This was done by comparing constant-current and potential-step measurements while monitoring the structural changes in the electrode with *in situ* XRD (**paper IV**).

Measurements were made at C/10 to study the electrochemical cell as close to equilibrium as possible. The (111) peak was monitored during reduction of the cell (Fig. 7.1 A). Two quasi-plateaus could be discerned: one distinct at 4.11 V and one more sloping, with an average potential of about 4.0 V (Fig. 7.2 A). The cell parameter for the single phase at SOD 0% coincides well with $Li_{1-x}Mn_2O_4$ (λ-MnO_2), while the phase at SOD 100% corresponds to $LiMn_2O_4$. [49] At SOD 0% a_c = 8.070 Å, and at SOD 100% a_c = 8.249 Å.

Faster constant-current measurements, corresponding to C/3 and 2C, were applied to the same electrochemical cell; the resulting discharge curves are shown in Figs. 7.2 B-C. A close to equal amount of charge was obtained for both C/10 and C/3 during discharge of the cell (Q ~ 2.50 mAh). For 2C the potentials are shifted towards a lower voltage, due to larger over-potential. The amount of charge passing through the cell at 2C was slightly less than at slower rates (Q = 2.47 mAh) and the capacity was 119.3 mAh/g.

The FWHM in a single-phase region is mainly determined by these factors:
(1) Instrumental broadening (here: 0.07-0.08° in 2θ).
(2) Particle-size broadening. Particles smaller than ~100 nm result in peak-broadening.
(3) Concentration gradients in the particles due to fast charge/discharge rates.
(4) Concentration gradients across the thickness of the electrode; a thick electrode may result in poorer material utilisation.
(5) Time resolution; an average over a longer time gives a broader peak in a dynamic electrochemical system.

In this study, (1), (2), and (5) are constant in the different measurements, leaving only (3) and (4) as a variable. Statement (4) can be assumed close to constant since the amount of charge obtained from the experiments at different current rates is almost equal.

If any Li concentration gradients would exist within the electrode material, it is expected that significant peak-broadening would be observed. No significant differences in FWHM were found here between the C/10, C/3 and 2C cases, indicating that no concentration gradient exists in the cell even at fast discharge rates.

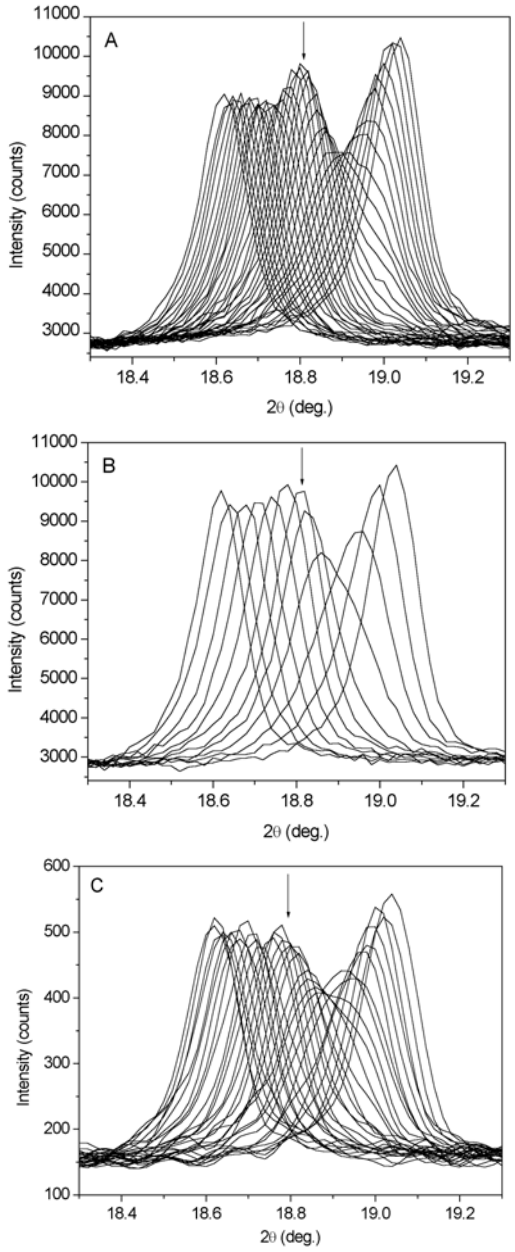

Figure 7.1 *In situ* XRD monitoring of the $LiMn_2O_4$ (111) peak during galvanostatic discharges. A. C/10. B. C/3. C. 2C.

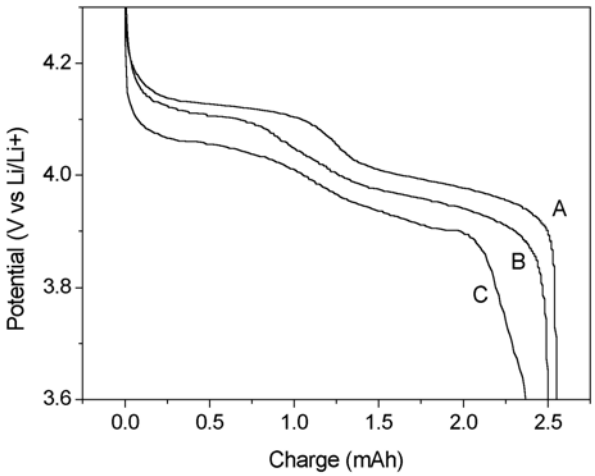

Figure 7.2 Discharge curves during the *in situ* measurements. A. C/10. B. C/3. C. 2C.

7.2 Potential steps

Current transients resulting from potential steps with various step-lengths are plotted in Fig. 7.3. Simulated curve-fits (dotted lines) are included in the same figure. The arrows indicate the point from which no further structural changes could be observed.

The time for the oxidation current response corresponds well with the time for the (111) peak to reach the 2θ position of λ-MnO_2 for the anodic potential-step, 3.6-4.3 V *vs.* Li/Li^+ (Fig. 7.3 A). There are two regions with different slopes in the I-t curve, one steeper in the upper part of the transient, and one flatter at the end of the transient. According to the XRD data, this change in slope occurs close to the rearrangement at SOD 50%. A potential step was applied in the reversed (cathodic) direction, *i.e.* 4.27 V to 3.60 V *vs.* Li/Li^+ (Fig. 7.3 B). In this direction, the current response has a higher initial value, and a shorter total relaxation time is needed to fully discharge the electrode. The integrated charge is, however, the same for both the anodic and the cathodic potential steps, and consistent with the value determined at C/10 from the pre-charge of the cell (2.52 mAh). However, a small amount of charge still passes through the cell, although the (111) peak has reached its final position at $LiMn_2O_4$, corresponding to approximately 2-3 % of the total capacity in the anodic step and ~9 % in the cathodic step.

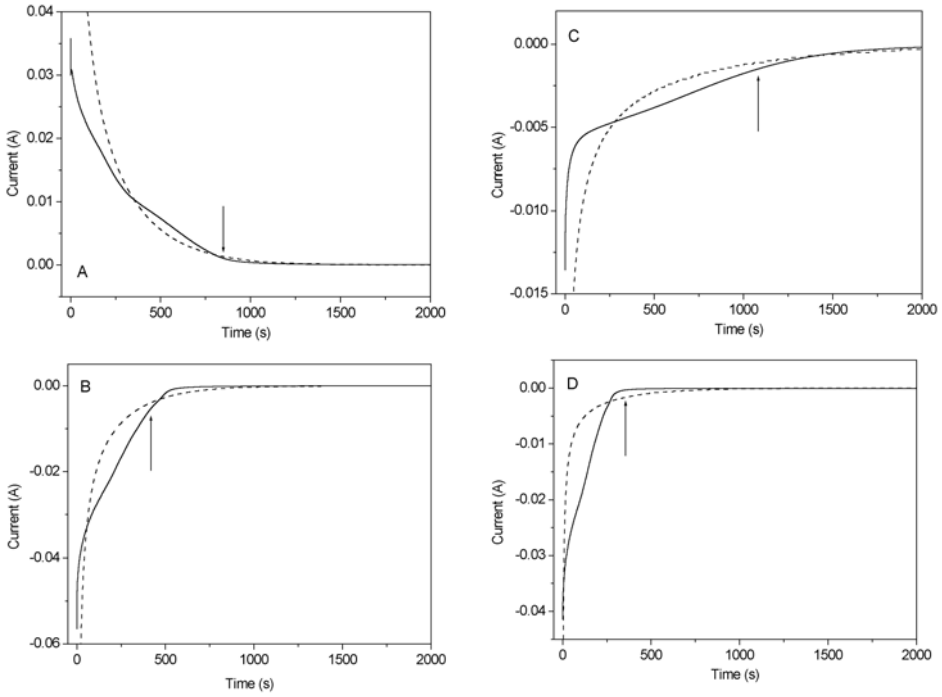

Figure 7.3 *In situ* Potential steps. A. 3.60-4.30 V. B. 4.22-3.60 V. C. 4.30-4.05 V. D. 4.05-3.60 V.

To monitor the behaviour of each of the two quasi-plateaus, the potential step was divided into two equally large steps: 4.24 V – 4.05 V *vs.* Li/Li^+, and 4.05 V – 3.60 V *vs.* Li/Li^+, corresponding to SOD 0-50% and SOD 50-100%, respectively. From these measurements, it can be seen that the relaxation time is longer when going from 0% to 50% SOD than when going from 50% to 100% SOD. This was confirmed by XRD (Figs. 7.4 C-D). There is still a current (corresponding to ~7 % of the total capacity) passing through the cell even after the diffraction peak has reached its final position in the SOD 0-50% step. This was not the case in the SOD 50-100% step. The amount of charge passing through the cell during these experiments was Q = 1.30 mAh for the SOD 0-50% step and Q = 1.22 mAh for the SOD 50-100% step, totally 2.52 mAh, consistent with the previous potential steps.

An applied potential step forces the potential at the surface of the particle of the active electrode material to become equal to the final potential, contrary to in a galvanostatic experiment. Consequently, the surface concentration would become equal to the corresponding final SOD momentarily or in a very short time after the step ($t<<1$ min). Thereafter, the electrode material relaxes continuously, making the concentration of the whole electrode material the same as that at the final SOD. It was thus expected that a potential step would result in a developed distribution of lattice parameters during the measured relaxation time. This was not observed for any of the potential steps applied.

On the contrary, the behaviour of the diffraction peak is similar to that observed for the galvanostatic cycling experiments, where the (111) peak moves continuously from SOD 0% to SOD 100%. The charge passing through the cell nevertheless corresponds well with that obtained at a slower constant-current cycling rate. The fact that no significant traces of the structure ($LiMn_2O_4$ or λ-MnO_2) corresponding to the final potential of the step can be seen before total relaxation indicates strongly that diffusion cannot be the rate-limiting step. From these observations, the suggested phase-boundary movement mechanism, proposed by Choi *et al.*, [121] can also be excluded as the rate-limiting process, since this mechanism would also result in a gradient.

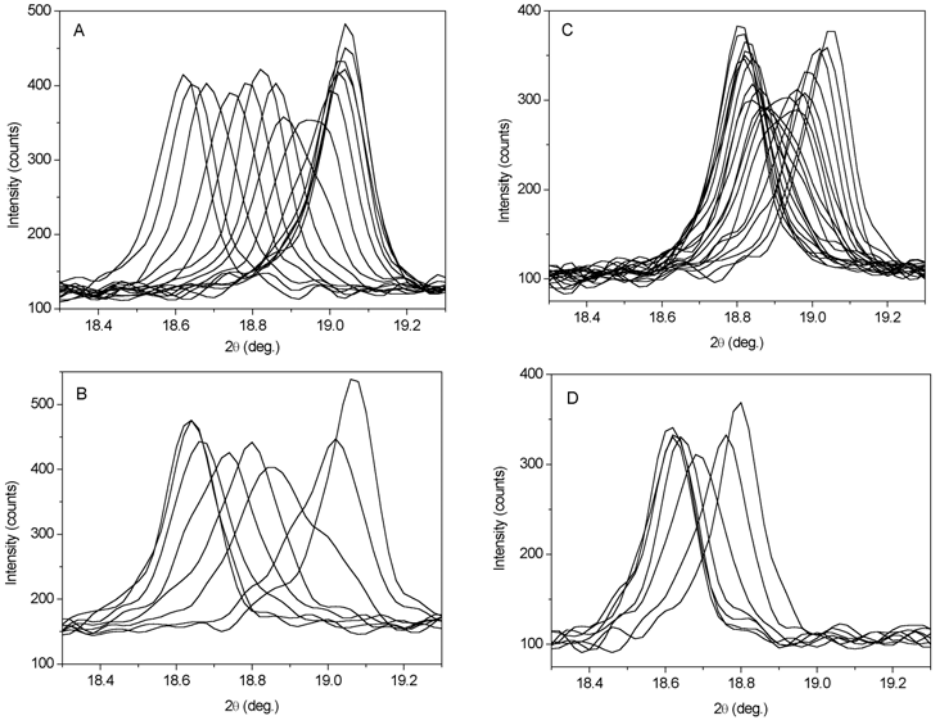

Figure 7.4 *In situ* XRD monitoring the $LiMn_2O_4$ (111) peak during the potential steps in Fig. 7.3. A. 3.6-4.3 V. B. 4.27-3.6 V. C. 4.24-4.05 V. D. 4.05-3.6 V.

Neither of the current transients shown in Fig. 7.3 behaves as Fick's law predicts. Instead, the behaviour of the transients, regarding the differences in shape and total relaxation time, seems to be strongly dependent on the potential. This therefore indicates that the rate-limiting process at high charge/discharge rates is also potential dependent. The two different regions in the transient slope for the potential step 3.6-4.3 V *vs.* Li/Li^+ could correspond to the two quasi-plateaus in the charge/discharge curve for $LiMn_2O_4$, and the observed change in slope may indicate a change in rate-limiting step or rate-constant.

The good utilisation of the cathode material in the 3.5-4.3 V *vs.* Li/Li^+ potential range even at high charge/discharge rates can be coupled to the ball-milling process used in the preparation of the cathode. Ball-milling may introduce significant strain effects and nano-sized regions in the active material. [58] This will affect the electrochemical performance of the cathode material.

8. CONCLUDING REMARKS AND FUTURE VISION

"Dream of Californication…"

- Red Hot Chilli Peppers

This thesis has been an effort to obtain a deeper understanding of the chemistry of the surface and bulk of $LiMn_2O_4$ in its application as a positive electrode in a Li-ion battery. This represents only a small piece in the puzzle but, for the system investigated, the electrode/electrolyte interface is one of the crucial trouble-spots. Anyone endeavouring to improve the electrode will hopefully be aided by this work.

A short summary of the conclusions that can be made from this work:

- A Li-rich and Mn^{3+}-rich surface phase is formed on $LiMn_2O_4$ electrodes during cycling and storage at ambient and elevated temperature.
- The oxidation products on $LiMn_2O_4$ electrodes at room temperature were found to be: LiF, Li_xPF_y (or Li_xBF_y) and poly(oxyethylene).
- The oxidation products on $LiMn_2O_4$ electrodes at 60°C are: LiF, $Li_xPF_yO_z$ (or $Li_xBO_yF_z$), phosphorous oxide (or boron oxides), poly(oxyethylen) and polycarbonate.
- The products formed on the electrodes are not governed by electrochemical cycling; however, they do depend on storage potential.
- A model for surface-film formation has been proposed.
- Solid-phase diffusion is not the rate-limiting step in $LiMn_2O_4$ electrodes.
- A good utilization of the electrodes was achieved by exploiting a ball-milling in electrode fabrication.

Eventhough there has been a lot of effort put into improving $LiMn_2O_4$, there are still problems to be overcome before the material can be commercialized. The question remains open as to whether the dissolution of Mn and the JT-transition can ever be controlled. If structural stability and corrosion problems can be circumvented, the high rate-capability but lack of high-temperature durability will make the material most appropriate for use in small electronic devices, while other materials with lower rate-capability but superior high-temperature performance will be more suited for electric-vehicle applications, *e.g.* $LiFePO_4$.

To avoid the formation of an SPI and on the positive electrode, it is necessary to prefabricate an inorganic barrier resembling the SEI on the cathode particles. This barrier must be impenetrable for solvent molecules but permit Li diffusion. There have only been a few attempts to achieve this so far. [73,79,80] More effort must be made in this area to make $LiMn_2O_4$ a viable commercial Li-ion cathode material.

ACKNOWLEDGEMENTS

Through my years as a PhD student, I have received extensive support from my supervisors Prof. Josh Thomas and Dr. Torbjörn Gustafsson. You have transformed me into a creative and self-supportive individual, for which I am very grateful.

To the people at the Department:
Ami – without our ventilating discussions, this thesis would never have been finished. Linda – my MISTRA ally through thick and thin. The other students from the "electrode group", past and present, who have helped and inspired me in my work. My "Rullan" lunch dates, you have introduced me to discussions beyond my imagination. My former room-mate Ludde for many interesting musical escapades. Those at the Department of Inorganic/Materials Chemistry who have arranged and attended the many ski-trips, parties, get-togethers, etc. The technical and administrative staff – you are quite indispensable!

A special thanks to Dr. Hikari Sakaebe who gave me back belief in my research and, during her year at our Department inspired me and taught me a lot about batteries and Japan. I promise I will visit you in Osaka one day…

To my collaborators within the MISTRA Programme:
It has been an interesting and enlightening experience to part in the National Programme: "Batteries and Fuel Cells for a Better Environment", both from a sociologic and scientific point of view. Anna-Karin – for your never-ending phone-calls. Cecilia – for your guiding hand through the IR jungle, and to the right restaurants in Gothenburg.

To the past and present staff at Danionics A/S for great support and know-how, and a never-ending supply of material.

To my friends outside the Chemistry sphere:
My old friends from Nyköping – you will always be very special for me. The Wallins – my second family. My friends from the undergraduate years in Uppsala – for all the fun we have had. Carro – for convincing me that Chemistry was the right path. The Nordlinders – for your immense hospitality during this final year.

To my family:
For always believing in me and supporting me, and especially for bringing me back to the real World every now and then.

To Sara: ♥

Uppsala, August 2001

REFERENCES

1. P.G. Bruce, in *Solid State Electrochemistry*, P.G. Bruce, Ed., Cambridge University Press, Cambridge, 1995.
2. E. Peled, *J. Electrochem. Soc.*, **126** (1979) 2047.
3. M.G.S.R. Thomas, P.G. Bruce, and J.B. Goodenough, *J. Electrochem. Soc.*, **132** (1985) 1521.
4. D. Guyomard, J.M. Tarascon, *Solid State Ionics*, **69** (1994) 222.
5. P. Arora, R.E. White, and M. Doyle, *J. Electrochem. Soc.*, **145** (1998) 3647.
6. *Handbook of Batteries*, 2nd edition, D. Linden, Ed., McGraw-Hill, Inc., New York (1995).
7. B. Scrosati, *Nature*, **373** (1995) 557.
8. S. Megahed and B. Scrosati, *Interface*, **4** (1995) 34.
9. D.E. Fenton, J.M. Parker, and P.V. Wright, *Polymer*, **14** (1973) 589.
10. M.B. Armand, J.M. Chabagno, and M.J. Duclot, Extended abstracts 2nd International Meeting on Solid Electrolytes, C.A. Vincent, Ed., St. Andrews University Press, St. Andrews, Scotland, 1978.
11. M.B. Armand, J.M. Chabagno, and J.M. Duclot in *Fast Ion Transport in Solids*, P. Vashista, J.N. Mundy, and G.K. Shenoy, Eds., Elsevier North Holland, New York, 1979, p. 131.
12. M.S. Whittingham, *Science*, **192** (1976) 1126.
13. M.B. Armand, in *Materials for Advanced Batteries*, D.W. Murphy, J. Broadhead, B.C.H. Steel, Eds., Plenum, New York, 1980, p.145.
14. T. Nagaura, K. Tozawa, *Prog. Batteries Sol. Cells*, **9** (1990) 209.
15. J.R. Dahn, T. Zheng, Y. Liu, and J.S. Xue, *Science*, **270** (1995) 590.
16. A.S. Gozdz, C.N. Schmutz, and J-M. Tarascon, U.S. Pat. 5,296,318 (1996).
17. N. Oyama, T. Tatsuma, T. Sato, and T. Sotomura, *Nature*, **373** (1995) 598.
18. P. Poizot, S. Laruelle, S. Grugeon, L. Dupont, and J-M. Tarascon, *Nature*, **407** (2000) 496.
19. D.W. Murphy and P.A. Christian, *Science*, **205** (1979) 651.
20. M. Winter, J.O. Besenhard, M.E. Spahr, and P. Novák, *Adv. Materials*, **10** (1998) 725.
21. R. Koksbang, J. Barker, H. Shi, and M.Y. Saïdi, *Solid State Ionics*, **84** (1996) 1.
22. A. Manthiram and J. Kim, *Chem. Mater.*, **10** (1998) 2895.
23. D. Abraham, presentation at CMM-MRL-UIUC, 28 Feb. 2001.
24. T. Ohzuku and A. Ueda, *Solid State Ionics*, **69** (1994) 201.
25. M.M. Thackeray, *Prog. Solid. St. Chem.*, **25** (1997) 1.
26. H. Berg, *Comprehensive Summaries of Uppsala Dissertations from the Faculty of Science and Technology*, **485**, Uppsala, 1999.
27. *Nonaqueous Electrochemistry*, D. Aurbach, Ed., Marcel Dekker, Inc, New York, 1999, and references therein.
28. K. Kanamura, S. Shiraishi, H. Takezawa, and Z. Takehara, *Chem. Mater.*, **9** (1997) 1797.
29. F. Kong, J. Kim, X. Song, M. Inaba, K. Kinoshita, and F. McLarnon, *Electrochem. Solid St. Lett.*, **1** (1998) 39.
30. A. Zaban and D. Aurbach, *J. Power Sources*, **54** (1995) 289.

31. A. Chu, J.Y. Josefowicz, and G.C. Farrington, *J. Electrochem. Soc.*, **144** (1997) 4161.
32. *Nonaqueous Electrochemistry*, D. Aurbach, Ed., Marcel Dekker, Inc, New York, 1999, p. 358.
33. D.H. Jang and S.M. Oh, *J. Electrochem. Soc.*, **144** (1997) 3342.
34. D. Aurbach, Y. Ein-Eli, B. Markovsky, A. Zaban, S. Luski, Y. Carmeli, and H. Yamin, *J. Electrochem. Soc.*, **142** (1995) 2882.
35. D. Aurbach, B. Markovsky, A. Schechter, Y. Ein-Eli, and H. Cohen, *J. Electrochem. Soc.,* **143** (1996) 3809.
36. D. Aurbach, M.D. Levi, E. Levi, and A. Schechter, *J. Phys. Chem. B*, **101** (1997) 2195.
37. A. Schechter, D. Aurbach, and H. Cohen, *Langmuir*, **15** (1999) 3334.
38. L.J. Krause, W.L. Lamanna, J. Summerfield, M. Engle, G. Korba, R. Loch, and R. Atanasoski, *J. Power Sources*, **68** (1997) 320.
39. D. Aurbach, B. Markovsky, I. Weissman, E. Levi, and Y. Ein-Eli, *Electrochim. Acta*, **45** (1999) 67.
40. K. Soga, S. Hosada, Y. Tazuke, S. Ikeda, *J. Polym. Sci., Poly. Lett.*, **14** (1976) 161.
41. P. Novák, P.A. Christensen, T. Iwasita, and W. Vielstich, *J. Electroanal. Chem.*, **263** (1989) 37.
42. K. Kanamura, S. Toriyama, S. Shiraishi, M. Ohashi, and Z. Takehara, *J. Electroanal. Chem.*, **419** (1996) 77.
43. D. Aurbach, M.D. Levi, E. Levi, H. Teller, B. Markovsky, G. Salitra, U. Heider, and L. Heider, *J. Electrochem. Soc.*, **145** (1998) 3024.
43. D. Aurbach, K. Gamolsky, B. Markovsky, G. Salitra, Y. Gofer, U. Heider, R. Oesten, and M. Schmidt, *J. Electrochem. Soc.*, **147** (2000) 1322.
44. A. Du Pasquier, A. Blyr, P. Courjal, D. Larcher, G. Amatucci, B. Gérand, and J-M. Tarascon, *J. Electrochem. Soc.*, **146** (1999) 428.
46. Y. Matsuo, R. Kostecki, and F. McLarnon, *J. Electrochem. Soc.*, **148** (2001) A687.
47. G. Hägg, *Allmän och Oorganisk Kemi*, Almquist & Wiksells, 1963.
48. R.J. Gummow, A. de Kock, and M.M. Thackeray, *Solid State Ionics*, **69** (1994) 59.
49. Joint Committee on Powder Diffraction Standards, Files 38-789 (λ-MnO_2), 35-782 ($LiMn_2O_4$), 38-299 ($Li_2Mn_2O_4$), 84-1634 (Li_2MnO_3), 46-810 ($Li_4Mn_5O_{12}$)
50. M.M. Thackeray, A. de Kock, M.H. Rossouw, D. Liles, R. Bittihn, and D. Hoge, *J. Electrochem. Soc*., **139** (1992) 363.
51. M.M. Thackeray, P.J. Johnson, L.A. de Picciotto, P.G. Bruce, and J.B. Goodenough, *Mat. Res. Bull.*, **19** (1984) 179.
52. M.M. Thackeray, W.I.F. David, P.G. Bruce, and J.B. Goodenough, *Mat. Res. Bull.*, **18** (1983) 461.
53. T. Ohzuku, M. Kitagawa, and T. Hirai, *J. Electrochem. Soc.*, **137** (1990) 769.
54. W. Liu, K. Kowal, and G.C. Farrington, *J. Electrochem. Soc.*, **145** (1998) 459.
55. Y. Xia and M. Yoshio, *J. Electrochem. Soc.*, **143** (1996) 825.
56. M.N. Richard, I. Keotschau, and J.R. Dahn, *J. Electrochem. Soc.*, **144**, 55 (1997).

57. X.Q. Yang, X. Sun, S.J. Lee, J. McBreen, S. Mukerjee, M.L. Daroux, and X.K. Xing, *Electrochem. Solid St. Lett.*, **2** (1999) 157.
58. S.-H. Kang, J.B. Goodenough, and L.K. Rabenberg, *Chem. Mater.*, **13** (2001) 1758.
59. A.R. Armstrong and P.G. Bruce, *Nature*, **381** (1996) 499.
60. H. Björk, T. Gustafsson, J.O. Thomas, *Electrochem. Commun.*, **3** (2001) 187.
61. R.J Gummow and M.M. Thackeray, *J. Electrochem. Soc.*, **141** (1994) 1178.
62. J. C. Hunter, *J. Solid State Chem.*, **39** (1981) 142.
63. M.M. Thackeray, S. Yang, A.J. Kahaian, K.D. Kepler, E. Skinner, J.T. Vaughey, and S.A. Hackney, *Electrochem. Solid St. Lett.*, **1** (1998) 7.
64. J. Cho and M.M. Thackeray, *J. Electrochem. Soc.*, **146** (1999) 3577.
65. D.H. Jang, Y.J. Shin, and S.M. Oh, *J. Electrochem. Soc.*, **143** (1996) 2204.
66. Y. Gao and J.R. Dahn, *Solid State Ionics*, **84** (1996) 33.
67. J.M. Tarascon, W. McKinnon, F. Coowar, T. Bowmer, G. Amatucci, and D. Guyomard, *J. Electrochem. Soc.*, **141** (1994) 1421.
68. A.D. Robertsson, S.H. Lu, and W. Howard, *J. Electrochem. Soc.*, **144** (1997) 3505.
69. G.G. Amatucci, N. Pereira, T. Zheng, and J.-M. Tarascon, *J. Electrochem. Soc.*, **148** (2001) A171.
70. G. Ceder, Y.-M. Chiang, D.R. Sadoway, M.K. Aydinol, Y.-I. Jang; B. Huang, *Nature*, **392** (1998) 694.
71. J. Kim and A. Manthiram, *Nature*, **390** (1997) 265.
72. G.G. Amatucci, C.N. Schmutz, A. Blyr, C. Sigala, A.S. Gozdz, D. Larcher, and J.M. Tarascon, *J. Power Sources*, **69** (1997) 11.
73. G.G. Amatucci, A. Blyr, C. Sigala, P. Alfonse, J.M. Tarascon, *Solid State Ionics*, **104** (1997) 13.
74. A. Blyr, C. Sigala, G. Amatucci, D. Guyomard, Y. Chabre, and J-M. Tarascon, *J. Electrochem. Soc.,* **145** (1998) 194.
75. B. Ammundsen, G.R. Burns, D.J. Jones, and J. Rozière, *Chem. Mater.*, **7** (1995) 2151.
75. P. Endres, A. Ott, S. Kemmler-Sack, H.A. Mayer, H.-W. Praas, and K. Brandt, *J. Power Sources***, 69** (1997) 145.
77. B. Ammundsen, D.J. Jones, J. Rozière, H. Berg, R. Tellgren, and J.O. Thomas, *Chem. Mater.*, **10** (1998) 1680.
78. H. Mao and J.N. Reimers, U.S. Pat. 5,964,902 (1999).
79. E. Wang, D. Ofer, W. Bowden, N. Iltchev, R. Moses, and K. Brandt, *J. Electrochem. Soc.*, **147** (2000) 4023.
80. J. Cho, Y.J. Kim, T-J. Kim, and B. Park, *Chem. Mater.*, **13** (2001) 18.
81. S. Mukerjee, T.R. Thurston, N.M. Jisrawi, X.Q. Yang, J. McBreen, M.L. Daroux, and X.K. King, *J. Electrochem. Soc.*, **145** (1998) 466.
82. E. Levi, M.D. Levi, G. Salitra,, D. Aurbach, R. Oesten, U. Heider, and L. Heider, *Solid State Ionics*, **126** (1999) 109.
83. P. Strobel, M. Anne, Y. Chabre, M.R. Palacin, L. Seguin, G. Vaughan, G. Amatucci, and J.M. Tarascon, *J. Power Sources*, **81-82** (1999) 458.
84. W. Li, J.N. Reimers, and J.R. Dahn, *Solid State Ionics*, **67** (1993) 123.

85. G.G. Amatucci, J.M. Tarascon, and L.C. Klein, *J. Electrochem. Soc.*, **143** (1996) 1114.
86. J.R. Dahn, *Phys. Rev. B*, **44** (1991) 9170.
87. A.H. Whitehead, K. Edström, N. Rao, and J.R. Owen, *J. Power Sources*, **63**, (1996) 41.
88. C. D. Wagner, W. M. Riggs, L. E. Davis, J. F. Moulder, and G. E. Muilenberg, *Handbook of X-ray Photoelectron Spectroscopy*, Perkin-Elmer Corporation Physical Electronics Division, USA, 1979.
89. *Practical Surface Analysis*, Vol. 1, 1st ed., D. Briggs and M.P. Seah, Eds., John Wiley & Sons, Chichester, 1983.
90. *Principles of Instrumental Analysis*, D.A. Skoog and J.J. Leary, 4th ed., Saunders College Publishing, Orlando, 1992.
91. *Differential Scanning Calorimetry of Polymers*, V.A. Bershtein and V.M. Egorov, Ellis Horwood Limited, Chichester, 1994.
92. D. Aurbach, M. D. Levi, E. Levi, B. Markovsky, K. Gomolsky, R. Oesten, U. Heider, and L. Heider, in *Lithium Batteries*, S. Surampudi and R. Marsh, Eds., PV 98-16, The Electrochemical Society Proceedings Series, Pennington, NJ, 1998, p. 173.
93. T. Eriksson, T. Gustafsson, and J. O. Thomas, in *Lithium Batteries*, S. Surampudi and R. Marsh, Eds., PV 98-16, The Electrochemical Society Proceedings Series, Pennington, NJ, 1998, p. 315.
94. D. Bar-Tow, E. Peled, and L. Burstein, *J. Electrochem. Soc.*, **146** (1999) 824.
95. D. Aurbach, I. Weissman, A. Schechter, and H. Cohen, *Langmuir*, **12** (1996) 3991.
96. S. Shiraishi, K. Kanamura, and Z. Takehara, *J. Electrochem. Soc.*, **146** (1999) 1633.
97. G.D. Khattak, M.A. Salim, L.E. Wenger, and A.H. Gilani, *J. Non-Cryst. Solids*, **262** (2000) 66.
98. T.J. Richardson, S.J. Wen, K.A. Striebel, P.N. Ross Jr., and E.J. Cairns, *Mater. Res. Bull.*, **32**, (1997) 609.
99. J.S. Foord and R.B. Jackman, *Philos. Mag. A*, **49** (1984) 657.
100. V. Di Castro and G. Polzonetti, *J. Electron Spectrosc. Relat. Phenom.*, **48** (1989) 117.
101. M.A. Stranick, *Surf. Sci. Spectra*, **6** (1999) 39.
102. M.A. Stranick, *Surf. Sci. Spectra*, **6** (1999) 31.
103. J. Töpfer, A. Feltz, D. Gräf, B. Hackl, L. Raupach, and P. Weissbrodt, *Phys. Status Solidi A*, **134** (1992) 405.
104. M. Oku, K. Hirokawa, and S. Ikeda, *J. Electron Spectrosc. Relat. Phenom.*, **7** (1975) 465.
105. M. Chigane and M. Ishikawa, *J. Electrochem. Soc.*, **147** (2000) 2246.
106. J.C. Carver, G.K. Schweitzer, and T.A. Carlson, *J. Chem. Phys.*, **57** (1972) 973.
107. N. Treuil, C. Labrugère, M. Menetrier, J. Portier, G. Campet, A. Deshayes, J-C. Frison, S-J. Hwang, S-W. Song, and J-H. Choy, *J. Phys. Chem. B*, **103** (1999) 2100.
108. N.V. Kosova, I.P. Asanov, E.T. Devyatkina, and E.G. Avvakumov, *J. Solid State Chem.*, **146** (1999) 184.

109. Y. Gao, M.N. Richard, and J.R. Dahn, *J. Appl. Phys.*, **80** (1996) 4141.
110. J.M. Tarascon, E. Wang, F.K. Shokoohi, W.R. McKinnon, and S. Colson, *J. Electrochem. Soc.*, **138** (1991) 2859.
111. H. Berg and J.O. Thomas, *Solid State Ionics*, **126** (1999) 227.
112. A.M. Andersson, K. Edström, *J. Electrochem. Soc.*, in press.
113. A. Du Pasquier, F. Disma, T. Bowmer, A.S. Gozdz, G. Amatucci, and J-M. Tarascon, *J. Electrochem. Soc.*, **145** (1998) 472.
114. M.N. Richard and J.R. Dahn, *J. Electrochem. Soc.*, **146** (1999) 2068.
115. L. Vogdanis, B. Martens, H. Uchtmann, F. Hensel, and W. Heitz, *Makromol. Chem.*, **191** (1990) 465.
116. S. Geniès, R. Yazami, J. Garden, and J.C. Frison, *Synth. Met.*, **93** (1998) 77.
117. T. Yoshihara, H. Todokoro, and S. Murahashi, *J. Phys. Chem.*, **41** (1964) 2902.
118. K. Meyer, *J. Non-Cryst. Solids*, **209** (1997) 227.
119. M.A. Salim, G.D. Khattak, and M. Sakhawat Hussain, *J. Non-Cryst. Solids*, **185** (1995) 101.
120. F. Joho and P. Novák, *Electrochim. Acta* , **45** (2000) 3589.
121. Y-M. Choi, S-I. Pyun, and J.M. Paulsen, *Electrochimica Acta*, **44** (1998) 623.